



Digital twinning of the human ventricular activation sequence to Clinical 12-lead ECGs and magnetic resonance imaging using realistic Purkinje networks for in silico clinical trials

Julia Camps^{a,*}, Lucas Arantes Berg^{a,1}, Zhinuo Jenny Wang^a, Rafael Sebastian^c, Leto Luana Riebel^a, Ruben Doste^a, Xin Zhou^a, Rafael Sachetto^d, James Coleman^a, Brodie Lawson^e, Vicente Grau^a, Kevin Burrage^{a,e}, Alfonso Bueno-Orovio^a, Rodrigo Weber dos Santos^b, Blanca Rodriguez^a

^a University of Oxford, Oxford, United Kingdom

^b Federal University of Juiz de Fora, Juiz de Fora, MG, Brazil

^c University of Valencia, Valencia, Spain

^d Universidade Federal de São João del Rei, São João del Rei, MG, Brazil

^e Queensland University of Technology, Brisbane, Australia

ARTICLE INFO

Keywords:

Cardiac digital twin
Purkinje network
Bayesian inference
Cardiac magnetic resonance

ABSTRACT

Cardiac in silico clinical trials can virtually assess the safety and efficacy of therapies using human-based modelling and simulation. These technologies can provide mechanistic explanations for clinically observed pathological behaviour. Designing virtual cohorts for in silico trials requires exploiting clinical data to capture the physiological variability in the human population. The clinical characterisation of ventricular activation and the Purkinje network is challenging, especially non-invasively. Our study aims to present a novel digital twinning pipeline that can efficiently generate and integrate Purkinje networks into human multiscale biventricular models based on subject-specific clinical 12-lead electrocardiogram and magnetic resonance recordings. Essential novel features of the pipeline are the human-based Purkinje network generation method, personalisation considering ECG R wave progression as well as QRS morphology, and translation from reduced-order Eikonal models to equivalent biophysically-detailed monodomain ones. We demonstrate ECG simulations in line with clinical data with clinical image-based multiscale models with Purkinje in four control subjects and two hypertrophic cardiomyopathy patients (simulated and clinical QRS complexes with Pearson's correlation coefficients > 0.7). Our methods also considered possible differences in the density of Purkinje myocardial junctions in the Eikonal-based inference as regional conduction velocities. These differences translated into regional coupling effects between Purkinje and myocardial models in the monodomain formulation. In summary, we demonstrate a digital twin pipeline enabling simulations yielding clinically consistent ECGs with clinical CMR image-based biventricular multiscale models, including personalised Purkinje in healthy and cardiac disease conditions.

1. Introduction

In silico clinical trials in cardiology is a novel approach to evaluating the safety and efficacy of therapies for cardiovascular diseases (Lim et al., 2020; Musuamba et al., 2021; Dasi et al., 2022; Roney et al., 2022). Human-based electrophysiological modelling and simulation can

enable identifying risk predictors from therapeutic options more accurately than animal models in some settings (Passini et al., 2017) and provide mechanistic explanations for clinically observed pathological behaviour (Roney et al., 2022; Margara et al., 2022; Dasí et al., 2023). Similarly to clinical trials, in silico clinical trials entirely rely on the patient cohort representing the variability that would be observed in the

* Corresponding author.

E-mail address: julcamps@gmail.com (J. Camps).

¹ Julia Camps and Lucas Arantes Berg made equal contributions to this work.

<https://doi.org/10.1016/j.media.2024.103108>

Received 23 June 2023; Received in revised form 6 February 2024; Accepted 13 February 2024

Available online 28 February 2024

1361-8415/© 2024 The Authors. Published by Elsevier B.V. This is an open access article under the CC BY license (<http://creativecommons.org/licenses/by/4.0/>).

human population that each treatment is targeting (Chang et al., 2017; Roney et al., 2022). A challenge in designing these virtual cohorts is the limited information available from clinical data and intersubject variability, requiring novel techniques to reduce and quantify model parameter uncertainty (Musumba et al., 2021). This uncertainty can be critical in highly inter-subject varying characteristics that have an essential role in the global performance of the heart but are poorly identified through existing clinical tests.

Clinical imaging such as cardiac magnetic resonance imaging (CMR) provides a rich, non-invasive characterisation of cardiac anatomy and structure, widely used in the development of digital twins (Giffard-Roisin et al., 2017; Lyon et al., 2018; Boyle et al., 2019; Roney et al., 2022). Moreover, the 12-lead electrocardiogram (ECG) is the most widely used clinical test, as it supplies a non-invasive characterisation of the cardiac cycle. In particular, the QRS complex of the ECG is the manifestation of the biventricular activation sequence, driven by the conduction system and the Purkinje network. Abnormalities in the Purkinje network are manifested in the QRS complex and are known to promote arrhythmic events and decrease pumping efficiency (Ideker et al., 2009; Haissaguerre et al., 2016). Exploiting the synergies of patient-specific imaging-derived anatomical and ECG-derived electrophysiological information using a digital twinning framework can improve the characterisation and reduce uncertainty on critical properties of the Purkinje network and ventricular activation sequences.

Our study aims to present a novel digital twin generation pipeline to integrate Purkinje networks efficiently in human multiscale ventricular models based on clinical magnetic resonance and 12-lead ECG data. Earlier studies have incorporated Purkinje networks in human cardiac models by combining subject-specific clinical data with physiological knowledge extracted from ex vivo experimental recordings (Kahlmann et al., 2017; Barber et al., 2021; Gillette et al., 2021; Correias et al., 2023). These studies considered reduced-order electrical propagation models based on the Eikonal equation, which can present limitations for in silico clinical trials due to their lack of biophysical detail. Therefore, here we focus on techniques that enable the development and calibration of biophysically detailed digital twin cohorts, including the Purkinje network, with clinical information available in large datasets, such as the UK Biobank (Sudlow et al., 2015). The pipeline incorporates a novel Purkinje generation strategy coupled with the inference of activation properties to enable variability in the Purkinje network structures in the virtual cohort. It also includes a translation strategy for building personalised biophysically detailed models from the reduced-order ones made by the inference strategy. We demonstrate the framework using clinical data of four healthy subjects and two patients with hypertrophic cardiomyopathy, a pro-arrhythmic disease, which can lead to anatomical and electrophysiological abnormalities and also affect the Purkinje network (Yokoshiki et al., 2014; Lyon et al., 2018).

2. Materials and methods

2.1. Digital twinning framework overview

The digital twinning framework combines a subject's CMR and ECG recordings to estimate a Purkinje network and a set of tissue conductivities that allow replicating the subject's QRS using a monodomain model of human-based electrophysiology. To this end, the framework first reconstructs a 3D geometry of the subject's heart suitable for electrophysiological simulations (Banerjee et al., 2021). Secondly, the framework uses reduced-order (Eikonal) simulations in combination with an inference strategy to estimate a set of earliest activation sites (root nodes for the Purkinje system) and conduction velocities (CV) that reproduce the subject's QRS (Camps et al., 2021). A novelty is the consideration of R wave progression as well as QRS morphology. Finally, the framework translates these root nodes and conduction velocities into a Purkinje network and a set of conductivities suitable for biophysically detailed (monodomain) simulations of human electrophysiology.

Thus, the digital twinning framework's flow chart (Fig. 1) is composed of the following subprocesses:

1. Automatic subject-specific mesh generation from CMR data (Banerjee et al., 2021).
2. Generation of consistent ventricular coordinates for the subject's CMR-based biventricular geometry (Appendix Section 8.2).
3. Sample a set of candidate endocardial root node locations to be considered by the inference (Section 2.2).
4. Calculate the distance between each candidate root node and the His-bundle while complying with human Purkinje anatomical evidence (Section 2.3).

Start of the inference of activation properties (Camps et al., 2021).

1. Generate the starting population of sets of root nodes and CVs by sampling the activation properties to be inferred and the root nodes with their distances to the His-bundle (Section 2.3).
2. Simulate the local activation time (LAT) maps for each parameter set (Section 2.5) in the population using the Eikonal model (Section 2.2) in combination with the prescribed activation properties (Section 2.5).
3. Calculate the 12-lead QRS complexes from each simulated LAT map (Section 2.2) using the torso-model-derived electrode positions (Section 2.10).
4. Apply the R wave-based normalisation in the calculated 12-lead QRS complexes. (Section 2.4)
5. Evaluate the discrepancies between the simulated and clinical data (Section 2.9).
6. Evaluate the objective (stopping) criteria to determine if the current population is a solution to the inference (Section 2.5).
7. (If criteria are not fulfilled) Update the population of parameter sets (Section 2.5), and continue from 5.
8. (If criteria are fulfilled) Choose the parameter set with the lowest discrepancy.

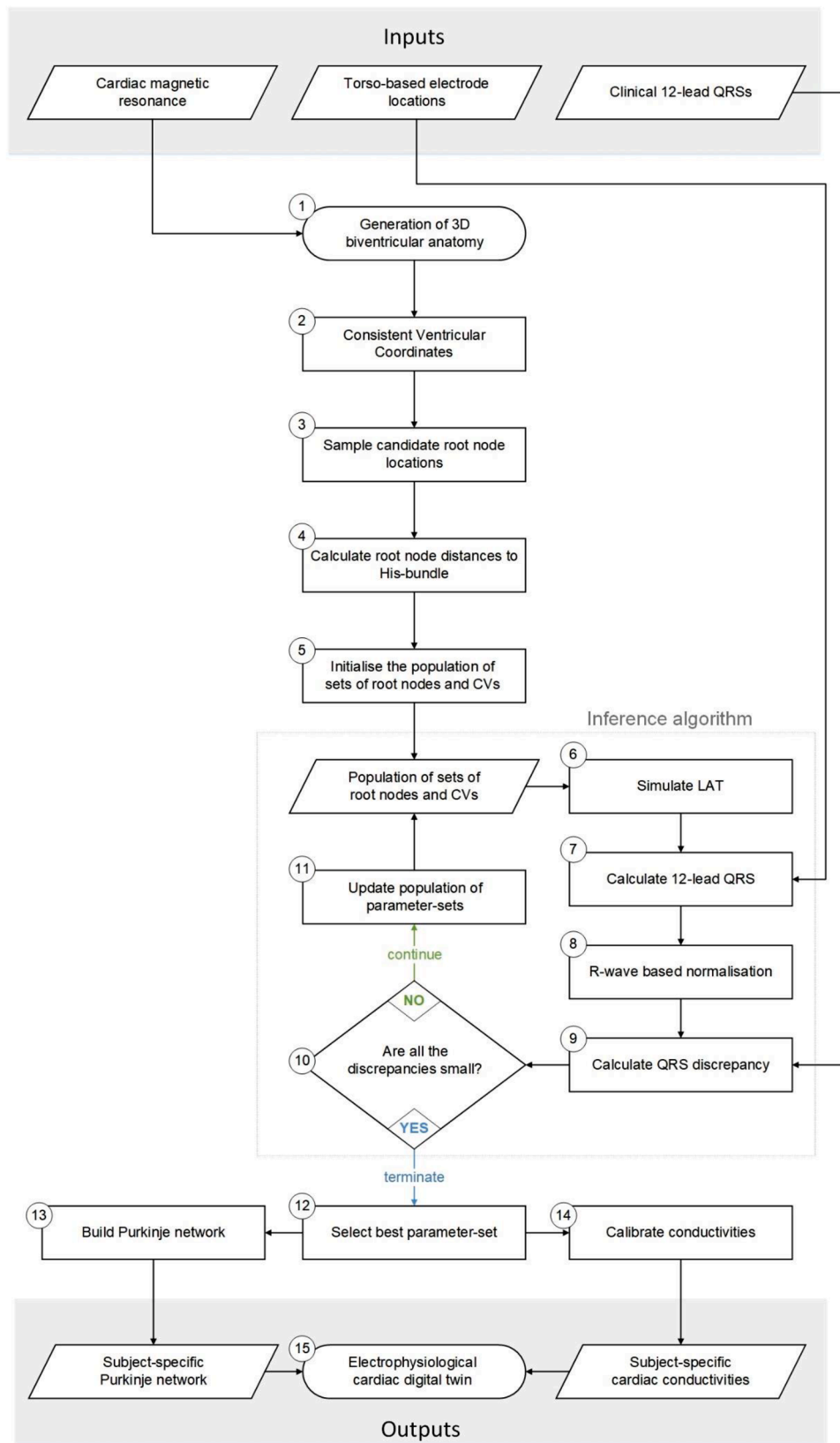
End of the inference of activation properties.

1. Build a biventricular Purkinje network model complying with the inferred root nodes (Section 2.7).
2. Calibrate the biophysical conductivities to the inferred conduction speeds using tissue slab simulations (Section 2.8).
3. Couple the Purkinje network, the biventricular geometry, with the human-based cellular models to produce a cardiac electrophysiological digital twin capable of reproducing the patient's 12-lead QRS complex.

2.2. Eikonal-based modelling and simulation for inferring root nodes and conduction velocities

Eikonal simulations were conducted for the inference of parameters determining ventricular activation sequence using Dijkstra's algorithm (Dijkstra, 1959), as described in Wallman et al. (2012). The biventricular mesh was considered a connected graph of 1.2 mm edge length, with traversal costs based on orthogonal longitudinal, transmural and transmural-normal conduction velocities (CVs) with respect to fibre orientation. Fibre orientations were generated using a rule-based method based on the finding from Streeter et al. (1969).

The endocardial (surface) layer was assigned fast isotropic CVs. Two CV values were considered in the fast endocardial layer, namely 'dense' and 'sparse', to account for the effect of spatial variations in the density of Purkinje-ventricular connections (Myerburg et al., 1972). 'Dense' and 'sparse' endocardial regions were defined using the apex-to-base (ab) and rotation-angle (rt) consistent ventricular coordinates. The 'dense' endocardial region covered the apical areas ($ab < 0.4$) in the left ventricle (LV) and the right ventricle (RV), plus the free-wall ($0.2 < rt <$



(caption on next page)

Fig. 1. Digital twin generation framework flow chart. The flow chart outlines the subprocesses comprising the electrophysiological calibration process for a subject given their CMR data, torso-based electrode locations, and clinical ECG. First, the 3D biventricular geometry is reconstructed from the CMR data. Secondly, the consistent ventricular coordinates are generated from the biventricular geometry. Next, the candidate root node locations are sampled by the inference method. Then, the distance between each root node and the His-bundle is calculated according to human Purkinje anatomical evidence. After this step, the population of the parameter set necessary for the inference to calculate the most suitable configuration for the conduction speeds and root nodes are initialised. Then, the inference algorithm begins. At each iteration, the Eikonal simulates the local activation times (LAT), and the pseudo-ECG algorithm calculates the simulated 12-lead QRS complexes; these are then normalised concerning the R wave progression in the subject's clinical ECG and then compared to this same clinical ECG. Finally, the parameter values defining the population of models are updated according to the discrepancy between the simulated and clinical ECGs. This process continues until the population discrepancy is smaller than the termination threshold, in which case, a model from the population is chosen for the biophysical calibration process. These models' parameter values are used to build a 3D Purkinje network and calibrate biophysical parameter values. The resulting calibrated biophysically detailed electrophysiological model, reproducing the subject's clinical QRS, is the final product of the calibration framework. The arrows determine the sequence of events in the flow chart. The shapes symbolise parallelograms – data; rectangles – processes; rhomboids – decisions. The grey background is used for the input and output data in the framework.

0.5) of the RV, while the rest of the endocardium was considered 'sparse' (Durrer et al., 1970; Myerburg et al., 1972).

The activation sequence was initiated based on root node locations and their activation times. These were determined by first generating branches that connected the root nodes to the His-bundle while following a set of rules extracted from data in the literature. Then, the distances between the His-bundle and each root node through their connecting branches were used in conjunction with the CV through the Purkinje network to calculate activation times at root nodes.

Two possible Purkinje fibres CVs were considered when determining the activation times at the candidate root nodes: 200 cm/s and 400 cm/s, reported as lower and upper bounds of physiological human Purkinje CV (Durrer et al., 1970; Myerburg et al., 1978; Rosen et al., 1981; Joyner and Overholt, 1985; Cragun et al., 1997; Maguy et al., 2009). Additionally, the case of simultaneous activation at the candidate root nodes was also evaluated, as performed by Camps et al. (2021).

The 12-lead ECG-QRS complexes were computed using the pseudo-ECG algorithm (Gima and Rudy, 2002). The QRS complex calculation was obtained by combining the activation time map with a step function to emulate the action potential upstroke.

2.3. Purkinje-based root node activation times

The Purkinje-myocardial junctions in humans are mainly located sub-endocardially (Vigmond and Stuyvers, 2016; Garcia-Bustos et al., 2019), and thus we considered endocardial locations for the root nodes. The algorithm for defining the root node activation times (Camps et al., 2022) is depicted in Algorithm 1 and hereafter described. Endocardial surfaces were sampled to obtain equidistant root nodes (2.5/1.5 cm apart, RV/LV) in both cavities. Secondly, Cobiveco ventricular coordinates were considered as transventricular (tv) [0, 1] (binary variable), apex-to-base (ab) [0 – 1] (float variable) and rotation-angle (rt) [0 – 1] (float variable) coordinates (Fig. A1) as in (Schuler et al., 2021) (Appendix Section 8.2). Thirdly, the His-bundle was defined in each endocardial surface at the mid-septal-basal point [$ab = 1$, $rt = 0.85$]. The LV and RV bundles are then defined by connecting each His-bundle to its respective apex at the mid-septal-apical point [$ab = 0$, $rt = 0.85$]. This structure serves as the baseline for our 'candidate' Purkinje network to compute root node activation times (Algorithm 1 lines 1–3). Next, five Cobiveco-based rules were defined on how to connect the candidate root nodes to the bundle (Fig. 2):

1. The candidate root nodes in the RV's ($tv = 1$) free-wall ($0.2 < rt < 0.5$) and apical ($ab < 0.2$) areas connect to the point in the non-basal bundle ($ab < 0.8$) that shares the most similar ab value to them. This creates a rib-caged pattern throughout the RV. (Fig. 2.1)
2. The LV's ($tv = 0$) apical ($ab < 0.4$) and septal ($0.7 < rt$) candidate root nodes connect to their closest apical ($ab < 0.4$) point in the LV bundle. (Fig. 2.2)
3. The non-apical RV's ($tv = 1$ & $ab > 0.2$) candidate root nodes that are in the septal ($0.7 < rt$) and paraseptal ($rt < 0.2 \mid 0.5 < rt < 0.7$)

Algorithm 1

Method for defining root nodes activation times.

Input parameters: Cobiveco ventricular coordinate system and candidate root nodes.

Output: Feasible root nodes connected to the His-bundle.

- 1 Define the His-bundle in each ventricle at the mid-septal-basal point [$ab=1$, $rt=0.85$];
- 2 Build the LV bundle branch by connecting the His-bundle to the LV apex at the mid-septal-apical point [$tv=0$, $ab=0$, $rt=0.85$];
- 3 Build the RV bundle branch by connecting the His-bundle to the RV apex at the mid-septal-apical point [$tv=1$, $ab=0$, $rt=0.85$];
- 4 **for each** candidate root node **do**
- 5 **if** ($tv = 1$ **and** $0.2 < rt < 0.5$) **or** ($tv = 1$ **and** $ab < 0.2$) **then**
- 6 RV-free-wall/RV-apical: Connect the point in the non-basal RV bundle ($ab < 0.8$) that shares the most similar ab value to the root nodes;
- 7 **else if** ($tv = 0$ **and** $ab < 0.4$) **or** ($tv = 0$ **and** $0.7 < rt$) **then**
- 8 LV-apical/LV-septal: Connect the closest apical point ($tv=0$ **and** $ab < 0.4$) to the LV bundle;
- 9 **else if** ($tv = 1$ **and** $ab > 0.2$) **and** ($rt < 0.2$ **or** $0.5 < rt < 0.7$) **then**
- 10 RV-septal-non-apical/RV-paraseptal: Connect the closest apical point ($tv=1$ **and** $ab < 0.2$) to the RV bundle;
- 11 **else if** ($tv = 0$ **and** $0.4 < ab$) **and** ($rt < 0.2$ **or** $0.5 < rt < 0.7$) **then**
- 12 LV-paraseptal-non-apical: Connect to the mid-paraseptal-apical point given by [$tv=0$, $ab=0.4$, $rt=0.1$] (posterior) or [$tv=0$, $ab=0.4$, $rt=0.6$] (anterior);
- 13 LV-paraseptal-non-apical: Connect to the closest point in the LV bundle ($ab < 0.4$);
- 14 **else if** ($tv = 0$ **and** $ab < 0.4$ **and** $0.2 < rt < 0.5$) **then**
- 15 LV-non-apical: Connect to the non-apical root node in the LV's free wall to the mid-free-wall-apical point [$tv=0$, $ab=0.4$, $rt=0.35$];
- 16 LV-non-apical: Connect to the closest point in the apical LV bundle ($ab < 0.4$);
- 17 **end-if-elseif**
- 18 **end-for**

regions also connect to their closest apical ($ab < 0.2$) RV bundle point. (Fig. 2.3)

4. The LV's ($tv = 0$) paraseptal-non-apical ($(0.4 < ab) \& (rt < 0.2 \mid 0.5 < rt < 0.7)$) candidate root nodes connect to their closest mid-paraseptal-apical point, [$tv = 0$, $ab = 0.4$, $rt = 0.1$] (posterior) or [$tv = 0$, $ab = 0.4$, $rt = 0.6$] (anterior), and from there to the closest point in the apical ($ab < 0.4$) LV bundle. (Fig. 2.4)
5. The non-apical candidate root nodes in the LV's free-wall ($tv = 0$ & $ab < 0.4$ & $0.2 < rt < 0.5$) connect to the mid-free-wall-apical point [$tv = 0$, $ab = 0.4$, $rt = 0.35$], then to their closest point in the apical ($ab < 0.4$) LV bundle. (Fig. 2.5)

Algorithm 1. Method for defining root nodes activation times. To generate feasible root nodes connected to the His-bundle, the input data is the following: the Cobiveco ventricular coordinate system and candidate root nodes covering both ventricles. The Cobiveco coordinates are defined as: transventricular (tv) [0, 1] - binary variable, apex-to-base (ab) [0, 1] - float variable, and rotation-angle (rt) [0, 1] - float variable. The result of the method is a set of root nodes that are connected to the His-bundle in both ventricles.

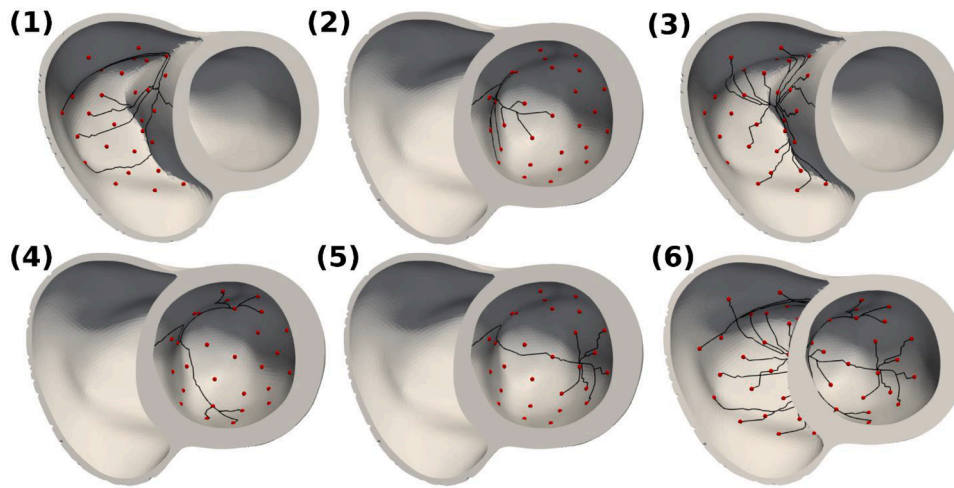


Fig. 2. Illustration of the endocardial rules used to link the LV/RV bundles to the root nodes, where the Purkinje network is coloured in black and the candidate root nodes in red. In panel (1), we are highlighting the first endocardial rule for the RV-free-wall/RV-apical, while in panel (2) the second rule for the LV-apical/LV-septal. Next, in panels (3), (4), and (5), we depict the third, fourth and fifth rules for the RV-septal-non-apical/RV-paraseptal, LV-paraseptal-non-apical and LV-non-apical regions, respectively. Finally, in panel (6), we show all the endocardial rules together with the corresponding root nodes.

With these routing rules, Dijkstra's algorithm was run on the endocardial surface to generate the paths between each candidate root node and His-bundle. This allows the calculation of the distances considered when activating the candidate root nodes. Finally, activation times at the candidate root nodes were quantified as their distance to the His-bundle divided by Purkinje fibres CV.

2.4. Strategies for ECG comparison

Simulated and clinical ECG comparison was conducted using a dynamic time warping-based algorithm (DTW) (Camps et al., 2021) combined with a novel R wave-based normalisation of the 12-lead ECG. The DTW algorithm effectively calculates differences between misaligned QRS complexes, which have been normalised using the information from the subject's clinical ECG recording. We extend it by including an R wave-based normalisation in addition to the QRS complexes morphology. The R wave progression of the 12-lead ECG is a well-established clinical biomarker for diagnosis. Furthermore, the R wave progression provides information on the dominant directions of the activation wavefront over time; thus, matching clinical R wave progression can give valuable information for developing cardiac digital twins.

For reporting our results, we adopted the mean \pm standard deviation of Pearson's correlation coefficient (Bear et al., 2018; Schaufelberger et al., 2019; Serinagaoglu Dogrusoz et al., 2019) as a measure of disagreement between our inference predictions and the 'target data' (i.e. clinical ECG).

2.5. Bayesian inference and parameter space

The inference method presented here extends Camps et al. (2021, 2022) to account for clinical ECG recordings and consider root nodes with activation time values given by a Purkinje-based model. Briefly, the inference method implements a sequential Monte Carlo approximate Bayesian computation algorithm (SMC-ABC) (Drovandi and Pettitt, 2011) to sample the parameters in the Eikonal model. It uses DTW-based discrepancy to compare the simulated and clinical ECG recordings iteratively, extended to consider R-progression across precordial leads. The iterative sampling continues until the objective criteria are fulfilled; namely, the population's discrepancy is smaller than a termination threshold (hyper-parameter).

We calibrated the hyper-parameters (e.g., the termination threshold,

the weights in the discrepancy metric, the maximum number of MCMC steps per iteration, etc.) used by the inference method using subject control-2 with Purkinje speed of 200 cm/s as a reference to enable matching clinical QRS signals. Subject control-2 was chosen for hyperparameter calibration because they displayed the median myocardial and torso volumes across the control subjects considered in this study. These hyperparameter values were then used in all subsequent inferences for the remaining five subjects and the other configurations for subject control-2. Nevertheless, we allowed the inference to run for as many iterations as required until the convergence (stopping) criteria were fulfilled in all cases.

The inference process was conducted under three different assumptions of the ventricular conduction system: Purkinje network with a CV of 200 cm/s (slow), Purkinje network with a CV of 400 cm/s (fast), and simultaneous activation at the root nodes (no Purkinje). These three configurations were chosen to represent the slow end of the spectrum in terms of reported CVs for the Purkinje network, the fast end of the spectrum (Durrer et al., 1970; Myerburg et al., 1972, 1978), and the effect of not considering a Purkinje network (Cardone-Noott et al., 2016).

The method inferred the value of three continuous parameters: endocardial 'dense' CV, endocardial 'sparse' CV, and transmural CV, as well as the discrete parameters representing the active root node locations. On the other hand, the CVs were considered constant along the longitudinal and transmural-normal direction of the fibres, 65 cm/s and 48 cm/s, respectively, as in Taggart et al. (2000), given their negligible effects on QRS simulations without conduction abnormalities (Camps et al., 2021).

The 'sparse' endocardial CV was allowed to adopt any value within the range [70 – 150 cm/s], the 'dense' CV was allowed to adopt values within [100 – 190 cm/s] (Durrer et al., 1970; Myerburg et al., 1972, 1978), and the transmural CV was allowed within the range [25 – 60 cm/s] (Caldwell et al., 2009; Durrer et al., 1970; Taggart et al., 2000). The number of candidate root nodes changed concerning the endocardial surface area in each geometry. The possible combinations of root nodes ranged from 1.2×10^{10} to 8.7×10^{11} for the smallest (Control-1) and largest (Control-4) biventricular geometries considered in this study.

The inference method considers a population of 512 parameter sets to allow for identifying different solutions to the inverse problem. The inference process has the capability of exploring the parameter space beyond the initial coverage of the sampling, thus not relying completely

on the initialisation of its population. However, to investigate the reproducibility of the inference results, we report three runs of the inference process per configuration considered in this study.

2.6. Monodomain-based modelling and simulation, including Purkinje network

Monodomain simulations were computed using the GPU-based solver MonoAlg3D (Sachetto Oliveira et al., 2018). The solver implements the finite volume method to solve the monodomain equation on the hexahedral biventricular meshes of the heart. Monodomain simulations were conducted using biophysically detailed models for human ventricular membrane kinetics (Tomek et al., 2019) and Purkinje membrane kinetics (Trovato et al., 2020). As in the Eikonal simulations, the monodomain ones also considered the rule-based method based on the finding from Streeter et al. (1969) for defining the orientation of the fibres. Based on a convergence analysis using the benchmark mesh from Niederer et al. (2011), which is detailed in Appendix Section 8.6, an 0.4 mm edge-length mesh resolution was considered and 0.4 mm thickness for the endocardial layer, following the same fibre orientation model as in the myocardium (Myerburg et al., 1978). Conductivities were adjusted for each subject following the guidelines presented in Appendix Section 8.3 to produce an agreement with their clinical QRS duration. This definition of the fast endocardial layer differed from the one considered in the Eikonal simulations. Thus, in the monodomain simulations, the fast endocardial layer will increase the conduction velocity globally, and the Purkinje network will be expected to reproduce the differences across the ‘dense’ and ‘sparse’ endocardial regions.

Monodomain simulations were conducted for three conduction system configurations:

‘Only root nodes’ considered only root nodes and no Purkinje network, similar to the Eikonal simulations employed by the inference process.

The ‘Minimal Purkinje network’ considers only the necessary Purkinje branches to connect to the root nodes.

The ‘Full Purkinje network’ includes further branches and Purkinje-myocardial junctions (PMJs).

In the ‘Only root nodes’ configuration, the activation sequence was initiated by electrical stimulation of endocardial root nodes. Each root node was modelled as a sphere in the endocardium ($duration = 4$ ms and $radius = 2$ mm) with current injected $I_{amp} = 53$ pA/pF. With the Purkinje network, the stimulus was injected as a single pulse at the proximal N_{cells} of the His-bundle with $I_{amp} = 40$ pA/pF, $duration = 4$ ms and $N_{cells} = 25$.

In the ‘Minimal Purkinje network’ and ‘Full Purkinje network’ configurations, the Purkinje network had an edge-length resolution of 0.1 mm (i.e., one hexahedral element).

In the monodomain equation, the surface-to-volume ratio was $\beta = 0.14 \mu m^{-1}$, and tissue capacitance was $C_m = 100$ pF/ μm^2 . A total simulation time of $t_{max} = 200$ ms was used, and a time discretisation $\Delta t = 0.01$ ms was used to solve the diffusion part of the model. To solve the reaction part associated with the Purkinje and ventricular cellular models, a Rush-Larsen scheme of first order was used (Gomes et al., 2020) with a fixed time step of $\Delta t = 0.01$ ms to solve the ordinary differential equations for the state variables.

Similarly to the Eikonal model, the QRS from the monodomain simulations were calculated using the simulated membrane potential values, also using a pseudo-ECG equation (Gima and Rudy, 2002).

2.7. Construction of human-based Purkinje network anatomical model

The generation of the minimal Purkinje networks for each subject required: (i) endocardial surfaces; (ii) inferred root nodes with their activation times; (iii) Purkinje CV considered in the inference; and (iv)

an error threshold (i.e., 1 ms) for the translation of the root node activation times. Next, the same rules previously used to define activation times at candidate root nodes were applied to find a new configuration of Purkinje branches (yielding negligible differences in their activation times) with no branches intersecting. The resulting minimal network connected the inferred root nodes to their ventricular bundle using geodesic lines on the surface of the endocardium. The minimal network from the RV and the LV were joined by their His-bundle, forming a biventricular Purkinje network that can be simultaneously stimulated at a single point and can propagate retrograde electrical waves across ventricles (Fig. 3.A).

The minimal Purkinje network is the baseline for generating a full Purkinje network that physiologically spans across the endocardium. Firstly, equidistant PMJ candidate locations are sampled (0.5/1 cm apart, dense/sparse) (Fig. 3.B). Secondly, the candidate PMJs are connected to the pre-existing Purkinje network one at a time using the algorithm presented in Berg et al. (2023) (Appendix 8.4), and the activation time of the PMJ is calculated. Only if the new activation time for the new PMJ differs by less than the error threshold (i.e., 2 ms) from the Eikonal simulated activation time for that location, then the new PMJ and branch are added to the pre-existing Purkinje network. Otherwise, the PMJ and its branch are discarded. This process is repeated for all the candidate PMJs, resulting in an expanded version of the minimal Purkinje network with greater coverage (Fig. 3.C). This strategy allows reproducing the inferred differences in the CV across the pre-defined ‘dense’ and ‘sparse’ regions as heterogeneities in the density of PMJs.

The Purkinje-myocardial coupling, which occurs at the PMJs, was modelled by including an additional resistor (R_{PMJ}) at the end of terminal branches, and its current I_{PMJ} was injected into tissue elements coupled to the terminal Purkinje elements as described in the following equation:

$$I_{PMJ} = \sum_{i=1}^{N_{PMJ}} \frac{(V_{purk} - V_{tiss_i})}{R_{PMJ}}$$

where V_{purk} is the transmembrane potential of the terminal Purkinje element, V_{tiss_i} is the transmembrane potential of the tissue element ‘i’ coupled to the Purkinje element, R_{PMJ} is a fixed resistance, and N_{PMJ} is the maximum number of tissue elements coupled to the Purkinje element, as can be seen in Fig. 4. This additional current is included on the right-hand side of the associated linear system of the ventricular domain only for the elements coupled to the Purkinje system.

The parameters R_{PMJ} and N_{PMJ} were calibrated to reproduce a physiological value for the characteristic 3–25 ms anterograde delay that occurs at the PMJ sites (Wiedmann et al., 1996). For all the monodomain simulations, the Purkinje coupling parameter values are set to $R_{PMJ} = 500k\Omega$ and $N_{PMJ} = 60$ following the same calibration protocol as in Berg et al. (2023).

2.8. Translation from Eikonal to monodomain

We translated the inferred myocardial and Purkinje network CVs from the Eikonal model by calibrating the conductivities in two monodomain tissue slab setups (Appendix Section 8.3). We calibrated a scaling factor over the myocardial conductivities for the inferred endocardial CVs using a binary search algorithm. This scaling factor was used to ramp up the CV in the fast endocardial layer with a thickness of 0.4 mm (one element thick) so that the resulting monodomain simulation matched the QRS duration observed in the subject’s clinical 12-lead ECG recording. This procedure was done irrespective of the ‘dense’ and ‘sparse’ endocardial regions. The CV differences across these regions were reproduced as changes in PMJ density. The calibrated conductivity values to the inferred conduction speeds using the monodomain tissue slab can be visualised in Table A1 Appendix Section 8.3. Regarding the cellular models, we use the ToR-ORD and Trovato models for human

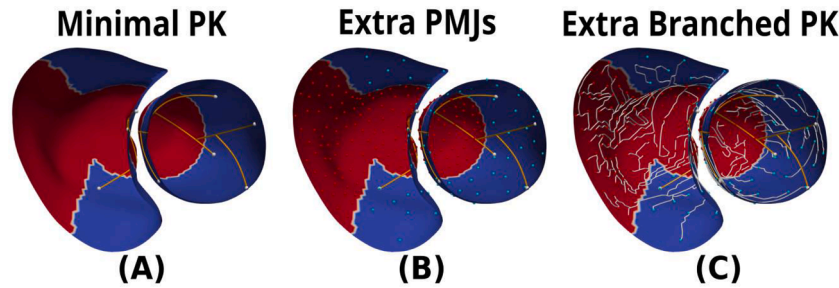


Fig. 3. Illustration of the extra branching procedure showing the different Purkinje network (PK) topology states. Next, new candidate PMJs are generated over the endocardium's dense (red) and sparse (blue) regions. Finally, the extra branching method is executed considering the minimal Purkinje network as an initial root, generating a dense Purkinje network that connects most of the candidate PMJs at a given error threshold.

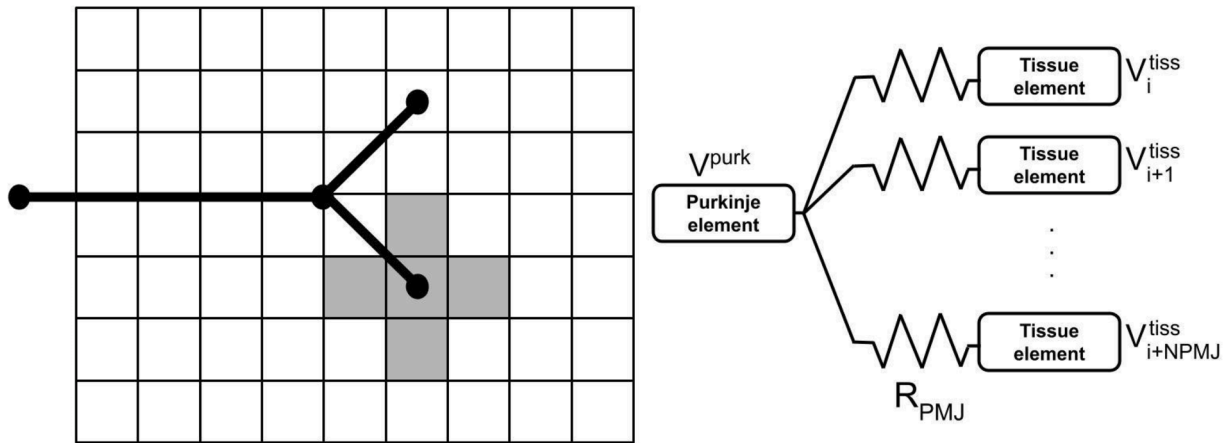


Fig. 4. Illustration of the Purkinje coupling model. The terminal Purkinje elements are linked to the nearest N_{PMJ} tissue elements by a fixed resistance R_{PMJ} , and an additional current I_{PMJ} is computed.

ventricular and Purkinje cells, respectively, as described in Section 2.6.

2.9. Metrics

To analyse and visualise our root node inference results, we map the errors on bull's eye plots (17 segments per ventricle) (Fig. A1 Appendix Section 8.2). We report local averaged errors between clinical and simulated QRSs as Pearson's correlation coefficient (PCC). We use a normalised (percentage) standard deviation ratio to compare the identifiability across different CVs being inferred. This metric will increase with the differences in the values predicted for each CV across the three repetitions of the inference.

2.10. Clinical data and data pre-processing

The digital twinning pipeline is demonstrated using clinical cine CMR and 12-lead ECG recordings from four control subjects and two HCM patients with distinct phenotypes (Lyon et al., 2018, 2018). The control subjects were selected to display significantly different heart and torso geometries, as in Mincholé et al. (2019), and numbered from one to four in increasing order of their myocardial volume. The HCM subjects had been identified to be representative of the phenotypic HCM subgroups 'group-1A' and 'group-3' (Lyon et al., 2018). Subject 'group-1A' had normal QRS morphology but inverted T-waves and apical and septal hypertrophy caused by repolarisation abnormalities. Subject 'group-3' had abnormally deep and wide S waves and septal hypertrophy, potentially explained by abnormalities in Purkinje-endocardial coupling in Lyon et al. (2018). These HCM subject subgroups are considered to have high arrhythmic risk. We generated the torso-biventricular 3D geometries from the CMR data (Banerjee

et al., 2021; Zacur et al., 2017) (Appendix Section 8.1). All geometries (both control and HCM) were considered to have no regional conduction abnormalities that would affect the activation sequence in the ventricles.

Target clinical ECG recordings were obtained by averaging 20 beats (Lyon et al., 2018) and manually delineating the resulting signals containing just the QRS complex. More precisely, the averaged QRS complexes resulting from the work by Lyon et al. (2018) included additional signals than the QRS and were misaligned across different leads. We corrected the misalignment and trimmed all QRS complexes to begin at the start of the Q wave and end at the end of the S wave while preserving a similar alignment for the R wave and while having the same signal length.

2.11. Computation and software

The inference for the six subjects was conducted with three repetitions to investigate the reproducibility of the results, resulting in 18 inferences. Each inference process required about 24 computation hours on a machine with $18 \times$ 2nd generation Intel Xeon Scalable Processors.

The inference pipeline was developed in Python/Numpy, and all the code developed for this study can be found at github.com/juliacamps/Cardiac-Digital-Twin-Purkinje. The algorithm to grow the biophysically detailed Purkinje network can be found at github.com/bergolho/Shocker. The monodomain simulations were performed with the GPU-based MonoAlg3D software, available at github.com/rsachetto/MonoAlg3D.C. The torso-biventricular meshes considered in this study are also available under request.

3. Results

3.1. Personalised Purkinje networks based on ECG and CMR clinical data

Fig. 5 and Table 1 demonstrate the ability of the computational pipeline presented above to deliver biophysically detailed biventricular models with Purkinje yielding simulated QRS complexes consistent with clinical ECGs for control subjects and diseased patients using both the Eikonal and monodomain models. Simulated and clinical QRS complexes were very similar in morphology and R progression, as illustrated in Fig. 5 for Control-2 and HCM Group 3 patients, and quantified in Table 1 for all cases ($PCC > 0.8$ for most configurations). Moreover, Fig. 5 demonstrates the method's ability to match the clinically observed R wave progression. The translation between Eikonal and monodomain simulations displayed consistent activation patterns for Control-2 as well as for HCM Group 3 subjects (Fig. 5.A-B); however, the latest activated region for the HCM Group 3 subject shifted slightly along the posterior wall between the Eikonal and monodomain (Fig. 5.B) due to the difference in formulation of the fast endocardial layer between these models. Nevertheless, the match to the ECG was preserved after this translation (Fig. 5.D). The best PCC values were achieved when considering either the Purkinje tissue conduction velocity of 400 cm/s (Table 1, Row 2) or the configuration with simultaneous activation at the root nodes (Table 1, Row 3). However, from comparing the values across different rows for each column, the differences between the average best configurations were smaller than 0.05 PCC in most cases, meaning that the inference was able to match the clinical ECG to a similar extent, considering different configurations for the Purkinje network.

3.2. Incorporation of Purkinje networks while preserving the simulated activation patterns

The patterns in the LAT map were preserved after incorporating the Purkinje stimulation protocol into our personalised monodomain simulations, as well as when extending the Purkinje network to cover the full cavity (Fig. 6). The QRS complexes simulated with the realistic

Purkinje networks displayed shorter durations compared to the simulations using the minimal Purkinje network and Only Root nodes setups (Fig. 6). From the results it can be observed that in the monodomain simulations with the Full Purkinje network, the QRS complexes are shorter than the clinical ones due to the electrotonic coupling effects from the additional PMJs, which speed up the already matched QRS width from the Minimal network.

Simulations using the baseline calibrated monodomain simulation with only root nodes stimulations versus incorporating the minimal Purkinje network achieved a similar PCC match to the clinical 12-lead QRS recordings (Fig. 7). Nevertheless, when expanding the network without further calibration of the monodomain model's parameters, a shortening of the QRS was observed and a subsequent decrease in PCC. The correlation between simulated and clinical QRS complexes using calibrated monodomain simulations was slightly lower than that obtained during the inference of the root nodes from the clinical QRS complex (Table 1).

3.3. All conduction velocities were similarly identified for the different configurations of the conduction system

Fig. 8 shows the CVs were inferred within physiological ranges, [25 – 60 cm/s] for the transmural, [100 – 190 cm/s] dense region and [70 – 150 cm/s] sparse region, for all control and disease subjects when using the Eikonal model (Table A1 Appendix Section 8.3). When the values for the standard deviation are averaged and calculated for each configuration and scenario, we obtain for the 'Transmural' a value of 11.95 cm/s, 12.60 cm/s and 12.95 cm/s for the 'SimultaRN', 'Pk200' and 'Pk400', respectively; for the 'Sparse' scenario the values are 20.55 cm/s, 18.16 cm/s and 21.13 cm/s, respectively; and for the 'Dense' the values are 28.55 cm/s, 25.46 cm/s and 21.59 cm/s.

Overall, from Fig. 8, we didn't identify different trends in the inferred conduction speeds between the control and HCM subject groups, except the transmural speed in the HCM Group 3 subject, for which we consistently inferred values of 60 cm/s. In general, there was no clear relationship between the percentage standard deviation scores amongst the inference experiments conducted regardless of the CV,

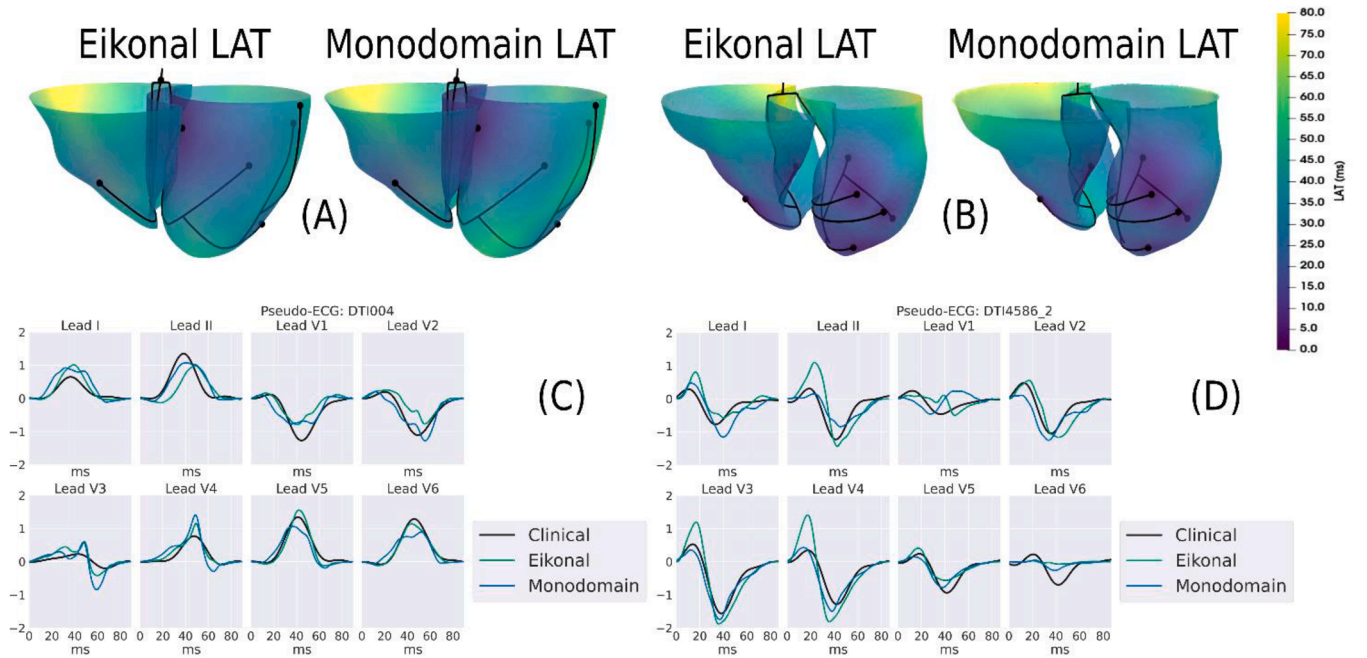


Fig. 5. Personalisation of human-based Purkinje network from clinical QRS and CMR for control and disease subjects. Comparison between simulated endocardial LATs from the inference's Eikonal solution and the monodomain simulations with a minimal Purkinje network (panels A and B for Control-2 and HCM Group 3, respectively). Comparison between simulated QRS complexes and clinical recordings for subjects Control-2 (C) and HCM Group 3 (D).

Table 1

Mean \pm standard deviation PCC values between clinical and inferred (using Eikonal equation) 12-lead QRS complexes for each subject and three configurations. Row 1: Purkinje network (PK) with a CV of 200 cm/s; Row 2: Purkinje with a CV of 400 cm/s; Row 3: simultaneously activated root nodes (RN). Abbreviations: PK – Purkinje; PCC – Pearson's correlation coefficient; RN – root nodes; HCM – Hypertrophic cardiomyopathy; std – corrected standard deviation.

PCC Mean (\pm std)	Control-1	Control-2	Control-3	Control-4	HCM Group 1A	HCM Group 3
PK 200 cm/s	0.77 (± 0.01)	0.89 (± 0.02)	0.89 (± 0.02)	0.88 (± 0.03)	0.91 (± 0.01)	0.79 (± 0.06)
PK 400 cm/s	0.81 (± 0.07)	0.91 (± 0.01)	0.90 (± 0.01)	0.89 (± 0.00)	0.93 (± 0.01)	0.75 (± 0.06)
Simultaneous RN	0.85 (± 0.03)	0.90 (± 0.00)	0.93 (± 0.02)	0.91 (± 0.02)	0.92 (± 0.01)	0.87 (± 0.01)

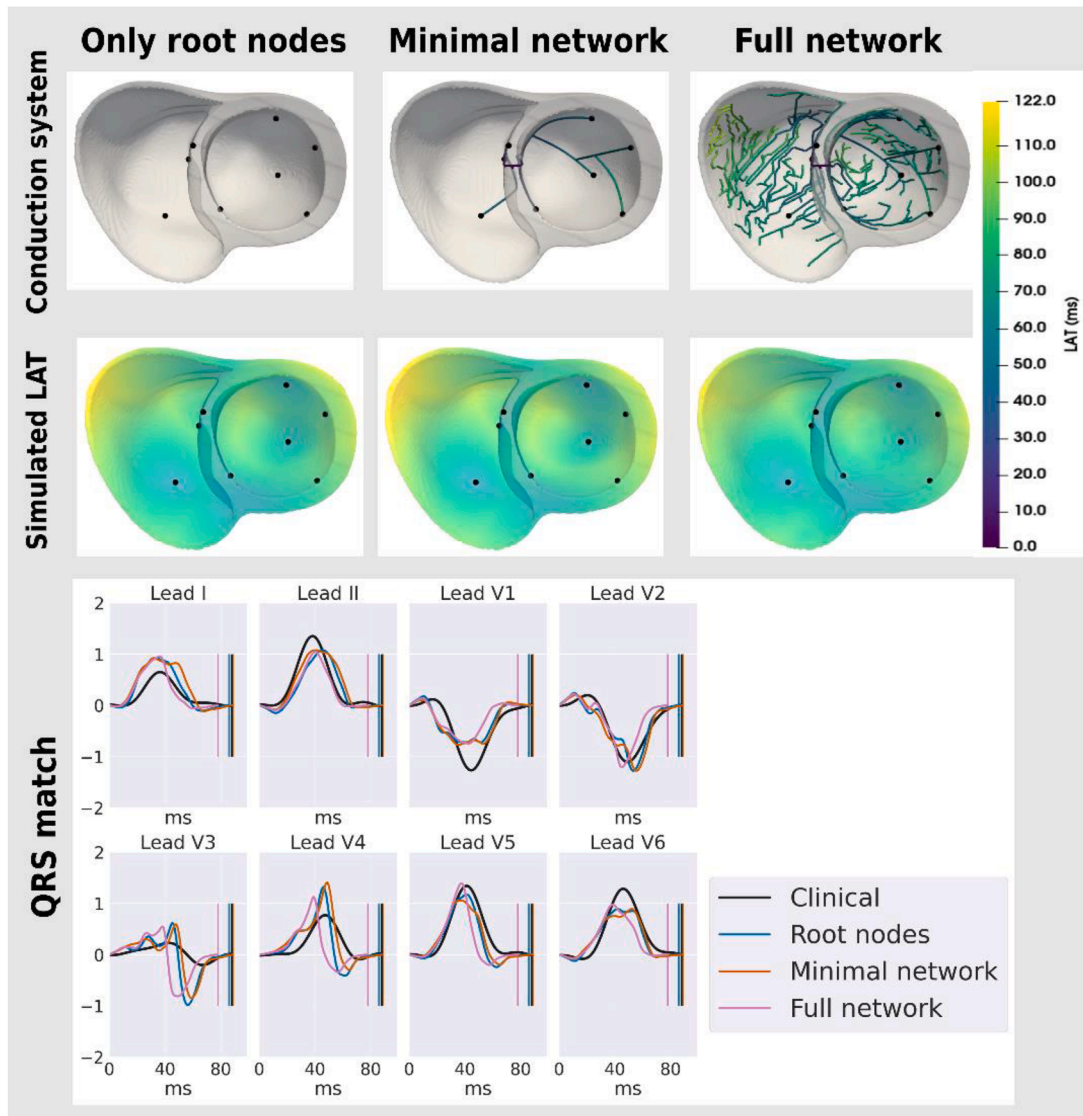


Fig. 6. Effect of the Purkinje network density on the personalised activation sequences in subject control-2 for monodomain simulations considering a Purkinje speed of 200 cm/s. The top row illustrates the modelling strategy for the conduction system: 'Only root nodes' (Root nodes) consider stimulation at the root nodes (black dots) at times prescribed after the inference; 'Minimal network' considers the necessary Purkinje network to connect the inferred root nodes to the His-bundle and uses this structure to stimulate the ventricles; 'Full Purkinje network' consider a Purkinje network that grows beyond the inferred root nodes. The middle row depicts the simulated LAT for each modelling strategy. Finally, the bottom row illustrates the simulated QRS complexes from 'Only root nodes' (blue), 'Minimal network' (orange), 'Full network' (pink), and the clinical QRS (black).

cardiac geometry, or stimulation protocol, suggesting similar identifiability capabilities of the CVs across these scenarios. Based on the calculated results from the standard deviation, we can conclude that the 'Transmural' is more identifiable than the 'Sparse,' which is more identifiable than the 'Dense' CVs. This observation is in agreement with the fact that the CVs from the 'Dense' region are the ones that demonstrate higher values and have more variability.

3.4. Distribution of root node locations is affected by the configuration of inferred CV values

For the control subjects, the inferred root nodes were scattered across the endocardium (Fig. 9). When considering simultaneous root nodes, no root nodes were estimated at the apex or mid to basal anterolateral regions, as can be seen in Fig. 6. The inferred locations of the root nodes were largely affected when we shifted the configuration to activation. In

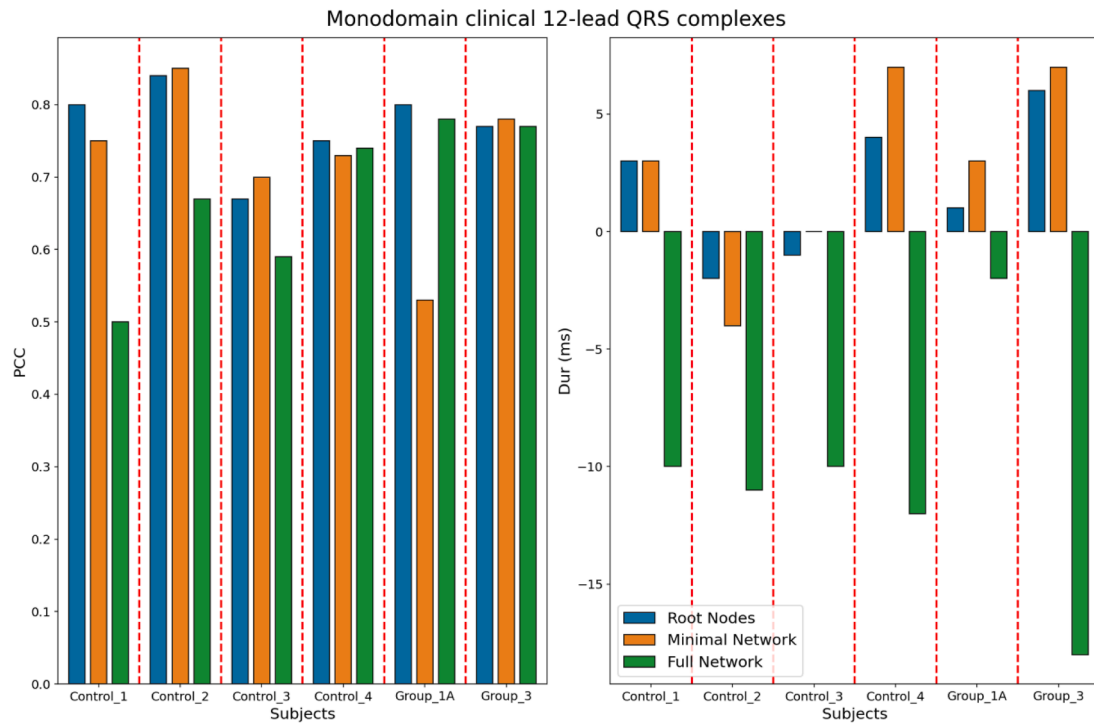


Fig. 7. Pearson correlation coefficients (PCC) and QRS Duration difference (Dur) between monodomain simulations and clinical 12-lead QRS complexes after calibrating the monodomain parameters to the results from the inference with Purkinje CV of 200 cm/s. In the left panel, each colour in the bar plot demonstrates the PCC when modelling the ventricular conduction system to a different extent, while in the right panel, the difference in QRS duration compared to the clinical signal is depicted. 'Only root nodes' (Root Nodes) – baseline calibrated monodomain simulation with stimulation only at the root nodes; 'Minimal network' – incorporates a Purkinje system that only connects from the His-bundle to the root nodes to the baseline setting and stimulates only at the His-bundle; 'Full network' - includes more branches to the Minimal network configuration that covers most of the endocardium.

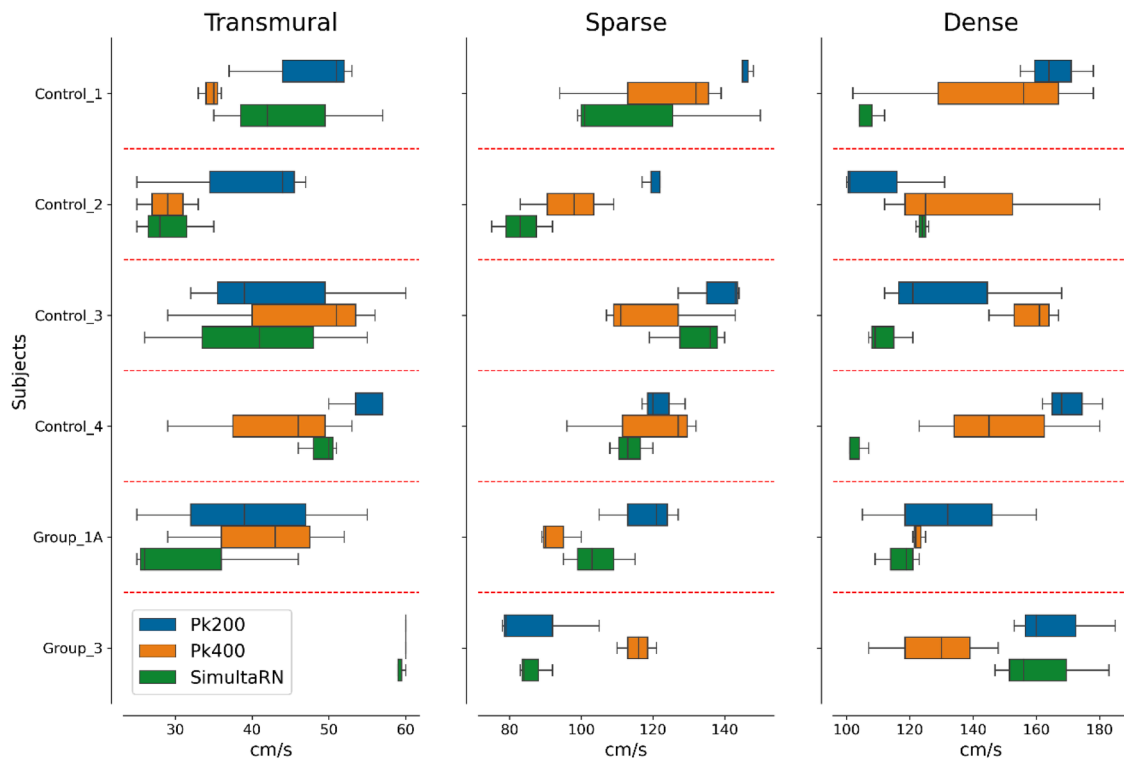


Fig. 8. Boxplot with the inferred CV values for each ventricular region (transmural fibre orientated, sparse and dense fast endocardial layer) considering each subject and their corresponding configuration when using the Eikonal model, where Pk200 is the configuration with a Purkinje CV of 200 cm/s, Pk400 with a Purkinje CV of 400 cm/s and SimultaRN when the root nodes are activated simultaneously. Note that the value of inferred transmural speed for the HCM Group 3 subject when considering the Purkinje tissue speed of 200 cm/s as well as 400 cm/s was 60 cm/s for all three repetitions of the inference in each of these configurations.

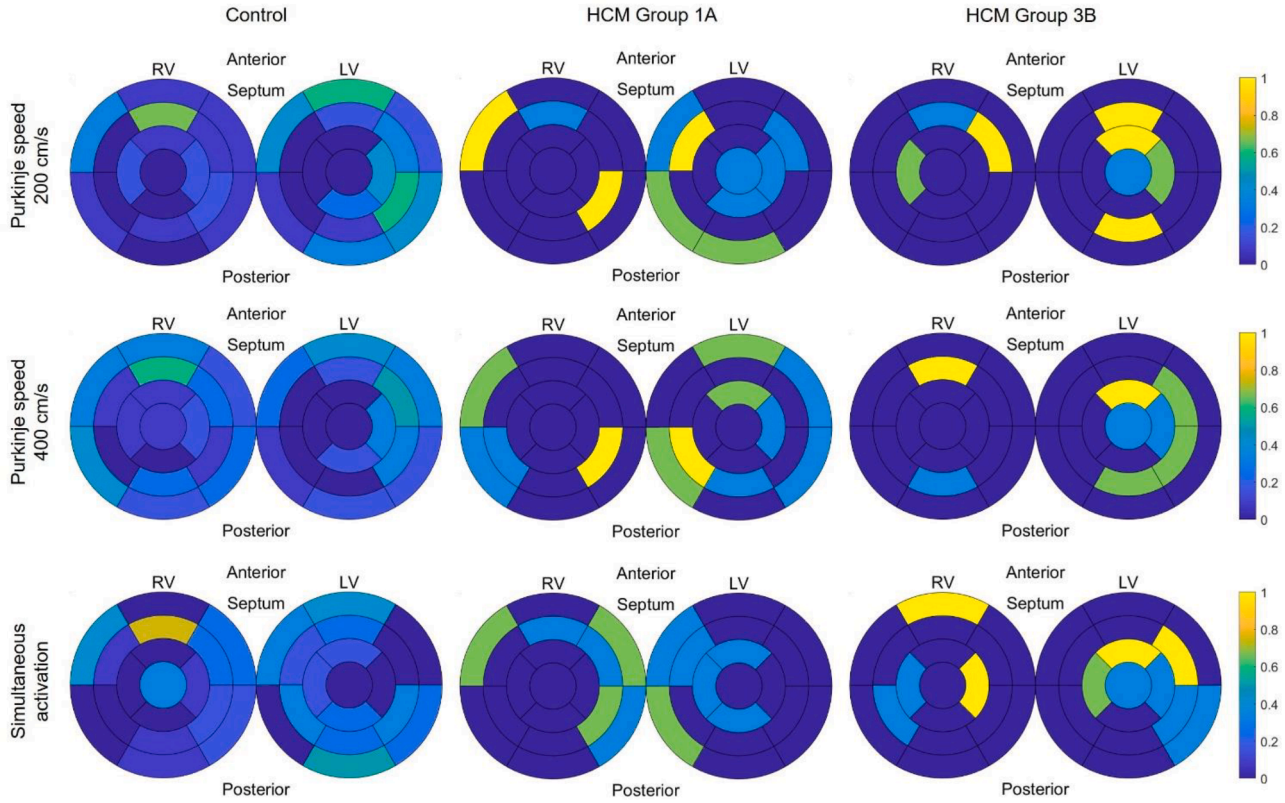


Fig. 9. Comparison of root node locations inferred in control and HCM subjects across all three inference runs per configuration using density maps. The colour map illustrated the percentage of times over the three runs of the algorithm when at least one root node was located in each quadrant/region of the 17×2 endocardial segment chart. The results are combined for all control subjects to be compared with the two representative HCM subjects.

addition, it is essential to notice that in Fig. 9, the results for all control subjects are combined to be compared with the two HCM groups. The average percentage of times when at least one root node was in a quadrant/region is calculated considering the four control subjects.

For the representative HCM subject from group 1A, characterised by having normal QRS morphology, the root nodes shifted from mainly being apical and septal-basal when Purkinje CV was 200 cm/s to anterolateral at the mid and basal when increasing Purkinje CV was 400 cm/s. These root nodes then moved from lateral to septal in both ventricles when the Purkinje CV was further increased to “simultaneous activation of the root nodes”. The HCM subject from group 3 initially displayed only apical root nodes symmetrically equidistant to the His-bundle. Then, when increasing the Purkinje CV, the inference method estimated more root nodes in the lateral wall, suggesting that the QRS phenotypes from the HCM subject from group 3 required a synchronised activation of apical and lateral regions.

The inferred root nodes from HCM subjects (group 3) were consistently located in the apex region, compared to other subjects (for every Purkinje CV and repetitions of the inference process), and produced deep-wide S-waves in the ECG. This result suggests that a predominantly apical root node location distribution combined with septal hypertrophy can be sufficient to reproduce the phenotypes observed in HCM subjects from group 3.

3.5. Simulating a dense Purkinje network speeds up the activation sequence through current injection and coupling effects

Our hypothesis is that during the monodomain simulations, current injection and subsequent electrotonic coupling effects had a major role in QRS shortening simulated from fully grown Purkinje networks compared to their smaller Minimal network counterparts (Fig. 6). The Full network grows using the Minimal network structure as a starting

point and the inference LAT result simulation from the Eikonal model as a target to grow additional branches and include new PMJs. Here, we test this hypothesis by disentangling the growth of the Full network from the Eikonal simulated LAT. Instead, we use the Minimal network’s simulation LAT to generate the Full Purkinje network. Without coupling effects, we would expect at most a 2 ms shortening of the QRS complex when extending the Purkinje network given by the LAT error threshold considered in our algorithm.

The differences in LAT patterns between stimulating the Root Nodes and the Minimal Network simulations were negligible (see Fig. 10). This was also true for their QRS complexes that had a PCC similarity of 0.99 and only a 1 ms difference in duration (Root Node simulation had 1 ms shorter QRS). This suggests that the stimulus protocol used for the root nodes is similar enough to have PMJs, justifying the translation from one to the other in our digital twin construction pipeline.

The inclusion of additional branches and PMJs to a minimal Purkinje network reduced the time to activate the ventricles by 8.3% (7 ms, from 84 to 77 ms), which was significantly higher than 2 ms (2.4%), i.e., the threshold allowed for additional PMJ (Fig. 10). This suggests that the coupling effects of the additional current delivered from the PMJs are aiding in depolarising neighbouring regions and thus causing a more significant effect than anticipated. On the other hand, we observed a slight slowdown in the activation times neighbouring the original root node locations (Fig. 10– LAT Diff to Minimal network, third row – third column). This suggests that increasing the network coverage can slightly slow down its CV. These differences resulted in a significant shortening of the QRS duration compared to the minimal network simulation (Fig. 10– QRS complexes); however, the PCC between these complexes remained at 0.97. All three modelling strategies for the cardiac conduction system obtained similar results to the minimal network configuration (Fig. 10) regarding QRS correlation.

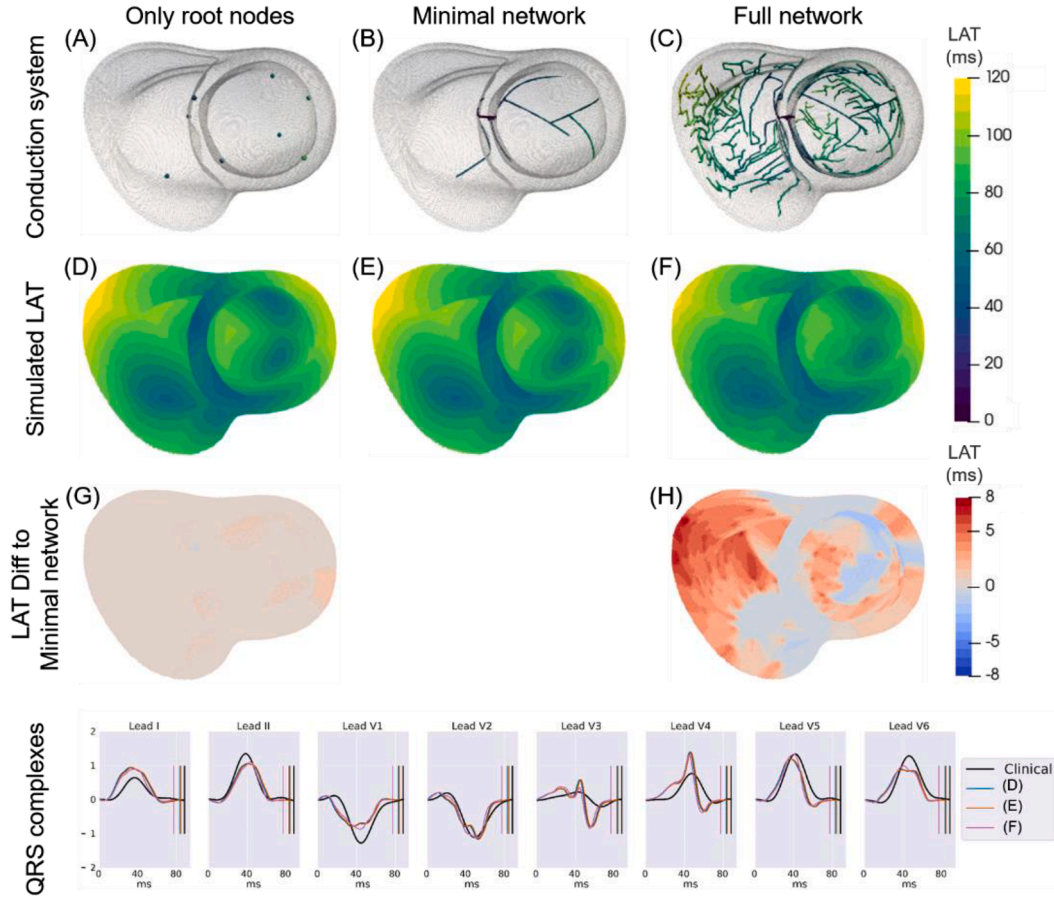


Fig. 10. Comparison of different formulations for the conduction system using the digital twins from control-2. The top row illustrates the modelling strategy for the conduction system: Only root nodes (A), Minimal Purkinje network (Minimal network) (B), and Full Purkinje network (Full network) (C). The second row illustrates the simulated LAT for each configuration considered (D-F). The third row illustrates the difference in simulated LAT maps: (G) between Only root nodes and Minimal network and (H) between Full and Minimal networks. Thus, positive values indicate that the Minimal network simulation was slower and negative values indicate that it was faster than the conduction systems in the other columns. The bottom row illustrates the simulated QRS complexes from Only root nodes (D, in blue), Minimal network (E, in red), Full network (F, in pink), and the clinical QRS (in black). The coloured vertical lines in the QRS complexes indicate the end of each signal to enhance the visualisation of differences in the simulated signal durations.

4. Discussion

We present a novel digital twin generation pipeline that combines (i) an ECG-guided inference method, (ii) human-based Purkinje representations, and (iii) an algorithm to extend inference-derived minimal Purkinje networks to realistic, fully grown ones. We also propose a strategy to translate the inference results using reduced-order models into biophysically detailed simulations that match subject-specific clinical recordings. Our pipeline can automatically build biophysically detailed digital twins from clinical CMR and ECG in about 36 h of computation time. This includes the CMR segmentation and mesh generation process (Banerjee et al., 2021), the Bayesian inference extended from (Camps et al., 2021), the Purkinje system modelling, and the calibration for biophysically-detailed simulations for in-silico trials and arrhythmia studies. An important novelty is the ability to match clinical QRS phenotypes beyond QRS duration. Furthermore, our pipeline is suitable for large datasets such as the UK Biobank (Sudlow et al., 2015), generating large cohorts of cardiac digital twins for in-silico trials. We demonstrate the flexibility of our methods and their power in explaining differences in QRS phenotypes across subgroups in the human population through personalisation of the activation sequence. The resulting digital twins matched the morphology and R wave progression of the subject's QRS complexes (Fig. 5) and enabled personalised mechanistic multiscale simulations. For reproducibility and verification, all codes are openly accessible through this publication.

Our work extends the capabilities of inference pipelines for digital twins in several respects. For example, Giffard-Roisin et al. (2017) estimated the location of just two root nodes in the left ventricle and the CVs from ECG data in a paced heart. Grandits et al. (2020) estimated the activation times of a known set of root nodes. Gillette et al. (2021) inferred activation and repolarisation parameters; however, they simplified the conduction system to have five fixed root nodes with simultaneous activation except for a root node in the free-wall (anchoring site of the moderator band), for which they estimated an activation delay constrained between zero and twenty-five milliseconds. Gillette et al. (2021) and Gillette et al. (2022) proposed strategies to extend their previous framework (Gillette et al., 2021) to include a realistic Purkinje network without modifying their inference machinery. Improving upon this, our method integrates the Purkinje network design as part of the inference process, using rules derived from human-based experiments in the literature as potential alternatives to initialise the parameter space. Then, it explores the resulting parameter space, which will have an approximate size of the order of 10^{12} possible combinations (number of root nodes, their locations and time delays), while also recovering the transmural and two fast endocardial CVs to match the subject's QRS complex in several different physiological ways. The biophysical Purkinje network generation algorithm utilised in this study extends the work of Berg et al. (2023) by considering the Minimal network as the initial network connecting the inferred root nodes to the His-bundle and constraining the extra PMJs to have the same LAT given

by the Eikonal inference simulation. These modifications enable preserving the match to the clinical QRS after growing the Purkinje network.

Additional contributions are, firstly, an algorithm for generating Purkinje networks using rules derived from the literature. Secondly, a strategy for expanding minimal Purkinje networks with PMJs covering all regions in the endocardium while preserving the match between clinical and simulated QRS complexes. Thirdly, an approach to represent the ventricular fast sub-endocardial layer that can mimic effects in the literature on regional heterogeneities of subendocardial conduction velocity through changes in the density of PMJs. This can enable the study of complex pro-arrhythmic wave-propagation behaviours, such as retrograde propagation through the cardiac electrical conducting system. Lastly, a strategy for calibrating biophysically detailed cardiac digital twins from Eikonal-based inference results using GPU-based monodomain simulations of human-based cardiac electrophysiology.

The inference method reproduces all QRS morphologies in diseased and healthy subjects with high fidelity, reporting PCC > 0.85 in at least one configuration of the cardiac conduction system for all subjects. This suggests that our method is flexible enough to represent pathological and healthy subjects without any perceptible biases on cardiac geometry or demographics. Moreover, our updated discrepancy metrics ensure that the resulting QRS complexes have a similar R-progression to the subjects, which improves the clinical relevance of the pipeline compared to our previous work (Camps et al., 2021). The inference method was able to reproduce the clinical characteristics of the QRS complexes even when varying the configuration of the Purkinje network (Table 1), suggesting that the specific characteristics of the Purkinje network may be a source of uncertainty when kept unchanged (Figs. 8 and 9). Further investigation on the effect of Purkinje tissue properties on the ECG may enable their personalisation from available clinical data.

In addition, the inference problem in this work considers a large continuous-discrete mixed parameter space, similar to Camps et al. (2021). However, the major difference in the parameter space for this work is the effect of the non-simultaneous activation of the root nodes. When activated simultaneously, the root nodes have a relative spatial influence on the QRS that depends on the proximity of other root nodes being activated. However, when considering non-simultaneous activations, the root nodes acquire an additional temporal relative influence on the QRS that depends on the activation time of the earliest root node to be chosen. More precisely, in this new formulation, the same root node will affect the QRS at different times depending on its chosen peers. This implies that the first reading in the QRS will come from the earliest root nodes selected in each parameter set. As a less significant difference, this new formulation of the problem allows root nodes not to be used when the activation front reaches the root node before its activation time. Thus, our method can sample ‘inactive’ root nodes. These differences in the parameter space resulted in a significantly more complex inference problem compared to when considering simultaneous activation at the root nodes in Camps et al. (2021).

We use population parameter sets during the inference to address the non-uniqueness of the solution to this inference problem. Furthermore, to prove the robustness of our results, we repeat the inference three times per configuration and make sure that our predictions are consistent across different runs of the software with different random initialisations of the environment variables. Moreover, the presented method produces a population of solutions to the inference of activation properties (Camps et al., 2021). However, for demonstration purposes, we only calibrated the biophysically detailed model to the solution with the lowest QRS discrepancy in the configuration, considering a Purkinje network speed of 200 cm/s.

In addition, we were able to calibrate biophysically detailed digital twins for each subject, preserving the high fidelity of the recovered activation sequences that matched the clinical QRS complexes (Fig. 8). The inclusion of a minimal Purkinje network in these cases preserved the match to the clinical data. Nevertheless, growing this network to be fully

sized accelerated the propagation of the activation wavefronts through electrotonic coupling effects (Fig. 6) and subsequently shortened the simulated QRS complexes. Suggesting a new correcting mechanism to counteract this effect is required while growing the Purkinje networks and increasing the number of PMJs in the ventricles. The incorporation of this Purkinje network enables the simulation of complex events such as retrograde propagation and the effects of treatment on the heart’s conduction system (Haissaguerre et al., 2016). These additional capabilities are key for the investigation of arrhythmic risk linked to the Purkinje network in-silico trials. Nevertheless, the modular nature of our pipeline also enables the production of digital twins without a coupled Purkinje network for the investigation of diseases and treatments that do not involve this network. The non-Purkinje subendocardial tissue can be faster at conducting electrical impulses compared to the rest of the myocardium (Myerburg et al., 1972), especially along the direction of the myocyte fibres in the endocardium (Myerburg et al., 1978) (in canine). The Purkinje network densely covers the endocardial layer in the ventricles and connects to the myocardium with reported densities (in pig hearts) of 0.33 – 0.55 PMJs per mm² (Garcia-Bustos et al., 2017). On the other hand, our inference method explores root nodes at a density of up to 1 root node per cm² and can only retrieve up to nine root nodes due to the computational complexity of the inference problem. Moreover, it is known that the density of the PMJs changes across different regions of the endocardium (Garcia-Bustos et al., 2017; Myerburg et al., 1972). Therefore, we defined two density regions based on experiments in Myerburg et al. (1972) since human Purkinje is more similar to canine than pig (De Almeida et al., 2015; Ono et al., 2009). We refer to the region with higher PMJ density as ‘dense’ and the region with lower PMJ density as ‘sparse’.

In our Eikonal simulations, we allow the fast endocardial CV in the ‘sparse’ and ‘dense’ regions to be different and isotropic. However, in our monodomain simulations, we define the fast endocardial layer to have a proportionally faster CV than the rest of the myocardium, as suggested by Myerburg et al. (1978). On the other hand, our monodomain simulations account for the differences in CV between these regions by increasing the density of PMJs in the ‘dense’ region compared to the ‘sparse’. The additional PMJs in the ‘dense’ region will increase the CV by two mechanisms: (1) PMJs can trigger earlier as they are connected through Purkinje tissue that is faster than the fast endocardial layer; thus, a region with additional PMJs will homogeneously activate earlier than without them. (2) The increment in stimulus current delivered from the additional PMJs will boost the depolarisation process in neighbouring tissue through diffusion and locally increase the functional CV during the activation sequence through electrotonic coupling. The effects of the fast endocardial scaling factor in different conditions on the transmural propagation of the wavefront and on the resulting QRS complexes are then evaluated.

A further experiment was done to evaluate the effect of the fast endocardial scaling factor (Appendix Section 8.5). From these results, we could notice no significant transmural differences in the propagation patterns due to the inclusion of the scaling factor across the different types of conduction systems; thus, the scaling factor had a similar effect to the Eikonal fast endocardial surface layer. In addition, there were minor differences in activation patterns between having only eight stimulation points at the root nodes compared to increasing this number to 1266 points, suggesting that the fast endocardial scaling factor is an appropriate phenomenological surrogate of a denser number of PMJs in our simulations as long as the activation patterns are already well represented. This is also supported by the similar QRS complexes computed from the simulations stimulated at eight and at 1266 locations, which have a PCC similarity of 0.95 (Fig. A2 Appendix Section 8.5).

On the other hand, increasing the number of PMJs by growing the Purkinje network to its full size had a larger effect on accelerating the activation sequence than anticipated (Fig. 6). We expected local increments in the fast endocardial CV because of increases in the density of PMJs. Our strategy was to emulate the CV difference between the

'sparse' and 'dense' regions in the monodomain simulations. However, including the additional PMJs reduced the QRS duration by up to five milliseconds more than the threshold for adding PMJs should allow, demonstrating the extent of the electrotonic coupling effect on the overall activation sequence. Nevertheless, the morphological traits of the QRS complexes from the minimal network simulation were improved in two subjects after growing the network (Fig. 6); thus, transitioning between these strategies can be done as a post-processing step after the inference process and may require small adjustments of the fast endocardial scaling factor to correct for the CV propagation resulting from the additional current delivered from new PMJs.

The results of the inference evaluation on control and HCM subjects demonstrate the great flexibility of our pipeline in representing varied phenotypes in any subject without tissue structural heterogeneities, such as scars. Interestingly, the inference recovered non-pathological values for the CVs and root node locations for the HCM subject with pathological deep-wide S-waves (group 3), suggesting that abnormal activation properties do not exclusively explain the deep-wide S-wave phenotype describing HCM group 3 but that it is also confounded by septal hypertrophy. We expanded on the findings from Lyon et al. (2018) using a targeted digital twin approach that reproduced the clinical data with higher fidelity and explored the parameter space in greater depth. According to our findings, no abnormalities in the conduction system of this subject would be required to reproduce its phenotypical QRS complexes. Nevertheless, given the multiple solution property of this inverse problem, it is uncertain what mechanism may underlie the activation sequence in this group of subjects. Future studies may expand on these findings, compare both mechanistic explanations of the phenotype to clinical and experimental data in the literature, and perform the inference in other subjects from the same phenotype subgroup. Finally, the novel pipeline can be a valuable tool for the calibration process of in-silico trials. For instance, given the patient-specific data, e.g., geometry and ECG, feasible candidates can be selected to replicate the given clinical data, which can be either healthy or under disease conditions.

4.1. Limitations

Some of the experimental data used to design the Purkinje strategy, the dense and sparse PMJ regions, and the fibre angle orientations in the heart were based on canine experiments. However, these designs are supported by the scarce data available from human experiments, with the exception of the dense PMJ region in the LV. Durrer et al. (1970) suggested that the dense PMJ region in the LV could be asymmetric between the anterior and posterior sides of the ventricle. However, given the limited amount of evidence on the shape of the dense region for the LV, we simplified it to be symmetric between the anterior and posterior of the ventricle, as suggested by the results in Myerburg et al. (1972). We used a generic configuration for cellular electrophysiology in our monodomain models for this study. In addition, the electrode locations are a source of uncertainty in our inference framework. These were not registered during acquisition and had to be recovered using the subject's torso geometries reconstructed from CMR data. A possible extension of our pipeline could account for the uncertainty in the electrode positions during the inference.

We observed that our inference method favoured the special case of simultaneous activation at the root node locations in terms of PCC match to the clinical QRS and computational cost of the inference process. We suspect the following explanation for this bias: ECG data was pre-processed individually for each lead to align the QRS because the averaging of the beats prevented an alignment of all leads together. This results in a loss of QRS timing differences that might inform activation delays between different spatial sites.

The fidelity of our simulated QRS complexes might have been affected by the uncertainty in electrode locations (Multerer and Pezzuto, 2021) and the distortion errors of the R wave amplitude from using a pseudo-ECG formulation (Nagel et al., 2022). While electrode location is

rarely registered in clinical practice, and any formulation of the ECG calculation will introduce some error in the results of the methodology, adopters of our digital twinning pipeline can consider known electrode locations and alternative formulations for the calculation of ECG signals without requiring any major changes to the current methods and software. These improvements could result in significantly enhanced matching to clinical QRS complexes.

Pre-defining the activation times at the root nodes constrains the possible structures the Purkinje network may adopt. While the current configuration already leads to a vast parameter space, additional flexibility would enable representing a population of plausible digital twins per subject that is more likely to include the actual subject's configuration. A possible extension of the current method could include fewer locations for the candidate root nodes while having each root node reached by more than one possible way from the His-bundle. Another strategy to reduce the uncertainty in the inferred Purkinje properties could be to incorporate additional data, such as endocardial intracardiac electrograms, when available (Barber et al., 2021). However, this should be left as an optional source of data since invasive measurements are less commonly available than 12-lead ECG and CMR recordings.

The current methodology for the growth of the Purkinje networks operates on the endocardial surfaces and does not allow branch intersection through the Purkinje topology. This limited the ability to represent the moderator bands and false tendons not bound to the endocardial surfaces. Nevertheless, the presented strategies can be easily extended to incorporate these new structures. (Barber et al., 2021)

4.2. Conclusions

We present a novel pipeline for the generation of biophysically detailed cardiac digital twins from CMR and ECG recordings capable of reproducing subject-specific QRS phenotypes in health and disease conditions. Our results demonstrate the need and power of complex digital twinning frameworks in reducing model calibration uncertainty through utilising available clinical data. Our framework can also augment these clinical data to improve risk stratification and mechanistic knowledge of poorly understood disease subgroups through mechanistically integrating multimodal clinical data. Applying this digital twinning framework to larger datasets, such as the UK Biobank, will enable the realisation of the vision for virtual human clinical trials.

CRediT authorship contribution statement

Julia Camps: Conceptualization, Data curation, Formal analysis, Investigation, Methodology, Software, Validation, Visualization, Writing – original draft, Writing – review & editing. **Lucas Arantes Berg:** Formal analysis, Investigation, Methodology, Software, Validation, Visualization, Writing – original draft, Writing – review & editing. **Zhinuo Jenny Wang:** Formal analysis, Methodology, Visualization, Writing – review & editing. **Rafael Sebastian:** Conceptualization, Methodology, Software, Supervision, Writing – review & editing. **Leto Luana Riebel:** Formal analysis, Investigation, Methodology. **Ruben Doste:** Data curation, Visualization, Writing – review & editing. **Xin Zhou:** Conceptualization, Investigation, Writing – review & editing. **Rafael Sachetto:** Resources, Software, Writing – review & editing. **James Coleman:** Formal analysis, Writing – review & editing. **Brodie Lawson:** Conceptualization, Methodology, Supervision, Writing – review & editing. **Vicente Grau:** Resources, Writing – review & editing. **Kevin Burrage:** Formal analysis, Supervision, Writing – review & editing. **Alfonso Bueno-Orovio:** Formal analysis, Writing – review & editing. **Rodrigo Weber dos Santos:** Conceptualization, Formal analysis, Investigation, Methodology, Supervision, Writing – review & editing. **Blanca Rodriguez:** Conceptualization, Funding acquisition, Project administration, Resources, Supervision, Writing – review & editing.

Declaration of competing interest

The authors declare the following financial interests/personal relationships which may be considered as potential competing interests:

Julia Camps reports financial support was provided by Engineering and Physical Sciences Research Council. Blanca Rodriguez reports financial support was provided by Wellcome Trust Fellowship in Basic Biomedical Sciences. Zhinuo Jenny Wang reports financial support was provided by CompBioMed 2 Centre of Excellence in Computational Biomedicine. Kevin Burrage reports financial support was provided by Australian Research Council Centre of Excellence for Mathematical and Statistical Frontiers. Kevin Burrage reports financial support was provided by Australian Research Council Discovery Project. Leto Luana Riebel reports financial support was provided by BBSRC PhD scholarship in collaboration with AstraZeneca. Rodrigo Weber dos Santos reports financial support was provided by Coordination of Higher Education Personnel Improvement. Rodrigo Weber dos Santos reports financial support was provided by National Council for Scientific and Technological Development. Rafael Sebastian reports financial support was provided by Generalitat Valenciana.

Data availability

I have included a link to the code in the manuscript and I will make the repository public after publication.

Acknowledgements

This work was funded by an Engineering and Physical Sciences Research Council doctoral award, a Wellcome Trust Fellowship in Basic Biomedical Sciences to Blanca Rodriguez (214290/Z/18/Z), an Oxford-BMS fellowship (R39207/CN063), the CompBioMed 2 Centre of Excellence in Computational Biomedicine (European Commission Horizon 2020 research and innovation programme, grant agreement No. 823712), the Australian Research Council Centre of Excellence for Mathematical and Statistical Frontiers (CE140100049), an Australian Research Council Discovery Project (DP200102101), by the Queensland University of Technology (QUT) through the Centre for Data Science, a BBSRC PhD scholarship in collaboration with AstraZeneca to Leto L. Riebel (BB/V509395/1), and by the Brazilian Government via CAPES, CNPq, FAPEMIG, UFSJ and UFJF, and Generalitat Valenciana Grant AICO/2021/318 (Consolidables 2021) and Grant PID2020-114291RB-I00 funded by MCIN/10.13039/501100011033 and by "ERDF A way of making Europe". The computation costs were incurred through two PRACE ICEI projects (icp013 and icp019), which provided access to Piz Daint at the Swiss National Supercomputing Centre, Switzerland. For the purpose of open access, the author has applied a Creative Commons Attribution (CC BY) public copyright licence to any Author Accepted Manuscript version arising from this submission.

Supplementary materials

Supplementary material associated with this article can be found, in the online version, at [doi:10.1016/j.media.2024.103108](https://doi.org/10.1016/j.media.2024.103108).

References

- Banerjee, A., Camps, J., Zacur, E., Andrews, C.M., Rudy, Y., Choudhury, R.P., Rodriguez, B., Grau, V., 2021. A completely automated pipeline for 3D reconstruction of human heart from 2D cine magnetic resonance slices. *Philos. Trans. R. Soc. A Math. Phys. Eng. Sci.* 379 (2212), 20200257 <https://doi.org/10.1098/rsta.2020.0257>.
- Barber, F., Langfield, P., Lozano, M., García-Fernández, I., Duchateau, J., Hocini, M., Haissaguerre, M., Vigmond, E., Sebastian, R., 2021. Estimation of personalized minimal Purkinje systems from human electro-anatomical maps. *IEEE Trans. Med. Imaging* 1. <https://doi.org/10.1109/TMI.2021.3073499>. –1.
- Bear, L.R., Dogrusoz, Y.S., Svehlikova, J., Coll-Font, J., Good, W., van Dam, E., Macleod, R., Abell, E., Walton, R., Coronel, R., Haissaguerre, M., Dubois, R., 2018. Effects of ECG signal processing on the inverse problem of electrocardiography. *Comput. Cardiol.* 2010, 45. <https://doi.org/10.22489/CinC.2018.070>.
- Berg, L.A., Rocha, B.M., Oliveira, R.S., Sebastian, R., Rodriguez, B., de Queiroz, R.A.B., Cherry, E.M., dos Santos, R.W., 2023. Enhanced optimization-based method for the generation of patient-specific models of Purkinje networks. *Sci. Rep.* 13 (1) <https://doi.org/10.1038/s41598-023-38653-1>. Article 1.
- Boyle, P.M., Zghaib, T., Zahid, S., Ali, R.L., Deng, D., Franceschi, W.H., Hakim, J.B., Murphy, M.J., Prakosa, A., Zimmerman, S.L., Ashikaga, H., Marine, J.E., Kolaidevelu, A., Nazarian, S., Spragg, D.D., Calkins, H., Trayanova, N.A., 2019. Computationally guided personalized targeted ablation of persistent atrial fibrillation. *Nat. Biomed. Eng.* 3 (11), 870–879. <https://doi.org/10.1038/s41551-019-0437-9>.
- Caldwell, B., Trew, M., Sands, G., Hooks, D., LeGrice, I., Smaill, B., 2009. Three distinct directions of intramural activation reveal nonuniform side-to-side electrical coupling of ventricular myocytes. *Circ. Arrhythm. Electrophysiol.* 2 (4), 433–440. <https://doi.org/10.1161/CIRCEP.108.830133>.
- Camps, J., Lawson, B., Drovandi, C., Mincholé, A., Wang, Z.J., Grau, V., Burrage, K., Rodriguez, B., 2021. Inference of ventricular activation properties from non-invasive electrocardiography. *Med. Image Anal.* 73, 102143 <https://doi.org/10.1016/j.media.2021.102143>.
- Camps, J., Wang, Z.J., Sebastian, R., Zhou, X., Lawson, B., Berg, L.A., Burrage, K., Grau, V., Weber, R., Rodriguez, B., 2022. Inference of number and location of purkinje root nodes and ventricular conduction properties from clinical 12-lead ECGs for cardiac digital twinning. *2022 Comput. Cardiol. (CinC)* 498, 1–4. <https://doi.org/10.22489/CinC.2022.235>.
- Cardone-Noott, L., Bueno-Orovio, A., Mincholé, A., Zemzemi, N., Rodriguez, B., 2016. Human ventricular activation sequence and the simulation of the electrocardiographic QRS complex and its variability in healthy and intraventricular block conditions. *EP Europace* 18 (suppl.4), iv4–iv15. <https://doi.org/10.1093/europace/euw346>.
- Chang, K.C., Dutta, S., Mirams, G.R., Beattie, K.A., Sheng, J., Tran, P.N., Wu, M., Wu, W., Colatsky, T., Strauss, D.G., Li, Z., 2017. Uncertainty quantification reveals the importance of data variability and experimental design considerations for in silico proarrhythmia risk assessment. *Front. Physiol.* 8. <https://www.frontiersin.org/articles/10.3389/fphys.2017.00917>.
- Correas, M., Guillem, M.S., Sánchez, J., 2023. Automated generation of purkinje networks in the human heart considering the anatomical variability. In: Bernard, O., Clarysse, P., Duchateau, N., Ohayon, J., Viallon, M. (Eds.), *Functional Imaging and Modeling of the Heart*. Springer Nature Switzerland, pp. 127–136. https://doi.org/10.1007/978-3-031-35302-4_13.
- Cragun, K.T., Johnson, S.B., Packer, D.L., 1997. β -adrenergic augmentation of flecainide-induced conduction slowing in canine Purkinje fibers. *Circulation* 96 (8), 2701–2708. <https://doi.org/10.1161/01.CIR.96.8.2701>.
- Dasi, A., Pope, M.T.B., Wijesurendra, R.S., Betts, T.R., Sachetto, R., Bueno-Orovio, A., Rodriguez, B., 2023. What determines the optimal pharmacological treatment of atrial fibrillation? Insights from in silico trials in 800 virtual atria. *J. Physiol. (Lond.)* 601 (18), 4013–4032. <https://doi.org/10.1113/JP284730>.
- Dasi, A., Roy, A., Bueno-Orovio, A., Rodriguez, B., 2022. Electrocardiogram metrics identify ionic current dysregulation relevant to atrial fibrillation. *Eur. Heart J.* 43 (Supplement 2) <https://doi.org/10.1093/eurheartj/ehac544.572> ehac544.572.
- De Almeida, M.C., Lopes, F., Fontes, P., Barra, F., Guimaraes, R., Vilhena, V., 2015. Ungulates heart model: a study of the Purkinje network using India ink injection, transparent specimens and computer tomography. *Anat. Sci. Int.* 90 (4), 240–250. <https://doi.org/10.1007/s12565-014-0255-9>.
- Dijkstra, E.W., 1959. A note on two problems in connexion with graphs. *Numer. Math. (Heidelberg)* 1 (1), 269–271. <https://doi.org/10.1007/BF01386390>.
- Drovandi, C.C., Pettitt, A.N., 2011. Estimation of parameters for macroparasite population evolution using approximate Bayesian computation. *Biometrics* 67 (1), 225–233. <https://doi.org/10.1111/j.1541-0420.2010.01410.x>.
- Durrer, D., Van Dam, R.Th., Freud, G.E., Janse, M.J., Meijler, F.L., Arzbacher, R.C., 1970. Total excitation of the isolated human heart. *Circulation* 41 (6), 899–912. <https://doi.org/10.1161/01.CIR.41.6.899>.
- García-Bustos, V., Sebastian, R., Izquierdo, M., Molina, P., Chorro, F.J., Ruiz-Sauri, A., 2017. A quantitative structural and morphometric analysis of the Purkinje network and the Purkinje–myocardial junctions in pig hearts. *J. Anat.* 230 (5), 664–678. <https://doi.org/10.1111/joa.12594>.
- García-Bustos, V., Sebastian, R., Izquierdo, M., Rios-Navarro, C., Bodí, V., Chorro, F.J., Ruiz-Sauri, A., 2019. Changes in the spatial distribution of the Purkinje network after acute myocardial infarction in the pig. *PLoS One* 14 (2), e0212096. <https://doi.org/10.1371/journal.pone.0212096>.
- Giffard-Roisin, S., Delingette, H., Jackson, T., Fovargue, L., Lee, J., Rinaldi, A., Ayache, N., Razavi, R., Sermesant, M., 2017a. Sparse Bayesian non-linear regression for multiple onsets estimation in non-invasive cardiac electrophysiology. In: Pop, M., Wright, G.A. (Eds.), *Functional Imaging and Modelling of the Heart*. Springer International Publishing, pp. 230–238. https://doi.org/10.1007/978-3-319-59448-4_22.
- Giffard-Roisin, S., Fovargue, L., Webb, J., Molléro, R., Lee, J., Delingette, H., Ayache, N., Razavi, R., Sermesant, M., 2017b. Estimation of Purkinje activation from ECG: an intermittent left bundle branch block study. In: Mansi, T., McLeod, K., Pop, M., Rhode, K., Sermesant, M., Young, A. (Eds.), *Statistical Atlases and Computational Models of the Heart. Imaging and Modelling Challenges*. Springer International Publishing, pp. 135–142. https://doi.org/10.1007/978-3-319-52718-5_15.
- Gillette, K., Gsell, M.A.F., Bouyssier, J., Prassl, A.J., Neic, A., Vigmond, E.J., Plank, G., 2021a. Automated framework for the inclusion of a his–Purkinje system in cardiac

- digital twins of ventricular electrophysiology. *Ann. Biomed. Eng.* 49 (12), 3143–3153. <https://doi.org/10.1007/s10439-021-02825-9>.
- Gillette, K., Gsell, M.A.F., Prassl, A.J., Karabelas, E., Reiter, U., Reiter, G., Grandits, T., Payer, C., Stern, D., Urschler, M., Bayer, J.D., Augustin, C.M., Neic, A., Pock, T., Vigmond, E.J., Plank, G., 2021b. A Framework for the generation of digital twins of cardiac electrophysiology from clinical 12-lead ECGs. *Med. Image Anal.* 71, 102080 <https://doi.org/10.1016/j.media.2021.102080>.
- Gillette, K., Gsell, M.A.F., Strocchi, M., Grandits, T., Neic, A., Manninger, M., Scherr, D., Roney, C.H., Prassl, A.J., Augustin, C.M., Vigmond, E.J., Plank, G., 2022. A personalized real-time virtual model of whole heart electrophysiology. *Front. Physiol.* 13. <https://www.frontiersin.org/articles/10.3389/fphys.2022.907190>.
- Gima, K., Rudy, Y., 2002. Ionic current basis of electrocardiographic waveforms: a model study. *Circ. Res.* 90 (8), 889–896. <https://doi.org/10.1161/01.RES.0000016960.61087.86>.
- Gomes, J.M., Oliveira, R.S., Lobosco, M., dos Santos, R.W., 2020. Adaptive-step methods for Markov-based membrane models. *Commun. Nonlinear Sci. Numer. Simul.* 85, 105249 <https://doi.org/10.1016/j.cnsns.2020.105249>.
- Grandits, T., Gillette, K., Neic, A., Bayer, J., Vigmond, E., Pock, T., Plank, G., 2020. An Inverse Eikonal Method for Identifying Ventricular Activation Sequences from Epicardial Activation Maps. *J. Comput. Phys.* 109700 <https://doi.org/10.1016/j.jcp.2020.109700>.
- Haissaguerre, M., Vigmond, E., Stuyvers, B., Hocini, M., Bernus, O., 2016. Ventricular arrhythmias and the His-Purkinje system. *Nat. Rev. Cardiol.* 13 (3) <https://doi.org/10.1038/nrcardio.2015.193>. Article 3.
- Ideker, R.E., Kong, W., Pogwizd, S., 2009. Purkinje fibers and arrhythmias. *Pacing Clin. Electrophysiol.* PACE 32 (3), 283–285. <https://doi.org/10.1111/j.1540-8159.2008.02232.x>.
- Joyner, R.W., Overholt, E.D., 1985. Effects of octanol on canine subendocardial Purkinje-ventricular transmission. *Am. J. Physiol.-Heart Circ. Physiol.* 249 (6), H1228–H1231. <https://doi.org/10.1152/ajpheart.1985.249.6.H1228>.
- Kahlmann, W., Poremba, E., Potyagaylo, D., Dössel, O., Loewe, A., 2017. Modelling of patient-specific Purkinje activation based on measured ECGs. *Curr. Dir. Biomed. Eng.* 3 (2), 171–174. <https://doi.org/10.1515/cdbme-2017-0177>.
- Lim, B., Kim, J., Hwang, M., Song, J.S., Lee, J.K., Yu, H.T., Kim, T.H., Uhm, J.S., Joung, B., Lee, M.H., Pak, H.N., 2020. In situ procedure for high-efficiency computational modeling of atrial fibrillation reflecting personal anatomy, fiber orientation, fibrosis, and electrophysiology. *Sci. Rep.* 10 (1) <https://doi.org/10.1038/s41598-020-59372-x>. Article 1.
- Lyon, A., Ariga, R., Mincholé, A., Mahmood, M., Ormondroyd, E., Laguna, P., de Freitas, N., Neubauer, S., Watkins, B., Rodríguez, B., 2018a. Distinct ECG phenotypes identified in hypertrophic cardiomyopathy using machine learning associate with arrhythmic risk markers. *Front. Physiol.* 9 <https://doi.org/10.3389/fphys.2018.00213>.
- Lyon, A., Bueno-Orovio, A., Zacur, E., Ariga, R., Grau, V., Neubauer, S., Watkins, B., Rodríguez, B., Mincholé, A., 2018b. Electrocardiogram phenotypes in hypertrophic cardiomyopathy caused by distinct mechanisms: apic-basal repolarization gradients vs. Purkinje-myocardial coupling abnormalities. *EP Europace* 20 (suppl_3), iii102–iii112. <https://doi.org/10.1093/europace/euy226>.
- Maguy, A., Le Bouter, S., Comtois, P., Chartier, D., Villeneuve, L., Wakili, R., Nishida, K., Nattel, S., 2009. Ion channel subunit expression changes in cardiac Purkinje fibers. *Circ. Res.* 104 (9), 1113–1122. <https://doi.org/10.1161/CIRCRESAHA.108.191809>.
- Margara, F., Psaras, Y., Wang, Z.J., Schmid, M., Doste, R., Garfinkel, A.C., Repetti, G.G., Seidman, J.G., Seidman, C.E., Rodríguez, B., Toepfer, C.N., Bueno-Orovio, A., 2022. Mechanism based therapies enable personalised treatment of hypertrophic cardiomyopathy. *Sci. Rep.* 12 (1) <https://doi.org/10.1038/s41598-022-26889-2>. Article 1.
- Mincholé, A., Zacur, E., Ariga, R., Grau, V., Rodríguez, B., 2019. MRI-based computational torso/biventricular multiscale models to investigate the impact of anatomical variability on the ECG QRS complex. *Front. Physiol.* 10 <https://doi.org/10.3389/fphys.2019.01103>.
- Multerer, M., Pezzuto, S., 2021. Fast and accurate uncertainty quantification for the ECG with random electrodes location. In: Ennis, D.B., Perotti, L.E., Wang, V.Y. (Eds.), *Functional Imaging and Modeling of the Heart*. Springer International Publishing, pp. 561–572. https://doi.org/10.1007/978-3-030-78710-3_54.
- Musuamba, F.T., Skottheim Rusten, I., Lesage, R., Russo, G., Bursi, R., Emili, L., Wangorsch, G., Manolis, E., Karlsson, K.E., Kulesza, A., Courcelles, E., Boissel, J.P., Rousseau, C.F., Voisin, E.M., Alessandrello, R., Curado, N., Dall'ara, E., Rodríguez, B., Pappalardo, F., Geris, L., 2021. Scientific and regulatory evaluation of mechanistic in silico drug and disease models in drug development: building model credibility. *CPT Pharmacometr. Syst. Pharmacol.* 10 (8), 804–825. <https://doi.org/10.1002/psp4.12669>.
- Myerburg, R.J., Gelband, H., Nilsson, K., Castellanos, A., Morales, A.R., Bassett, A.L., 1978. The role of canine superficial ventricular muscle fibers in endocardial impulse distribution. *Circ. Res.* 42 (1), 27–35. <https://doi.org/10.1161/01.RES.42.1.27>.
- Myerburg, R.J., Nilsson, K., Gelband, H., 1972. Physiology of canine intraventricular conduction and endocardial excitation. *Circ. Res.* 30 (2), 217–243. <https://doi.org/10.1161/01.RES.30.2.217>.
- Nagel, C., Espinosa, C.B., Gillette, K., Gsell, M.A.F., Sánchez, J., Plank, G., Dössel, O., & Loewe, A. (2022). *Comparison of propagation models and forward calculation methods on cellular, tissue and organ scale atrial electrophysiology* (arXiv:2203.07776). arXiv. 10.48550/arXiv.2203.07776.
- Niederer, S.A., Kerfoot, E., Benson, A.P., Bernabeu, M.O., Bernus, O., Bradley, C., Cherry, E.M., Clayton, R., Fenton, F.H., Garny, A., Heidenreich, E., Land, S., Maleckar, M., Pathmanathan, P., Plank, G., Rodríguez, J.F., Roy, I., Sachse, F.B., Seemann, G., Smith, N.P., 2011. Verification of cardiac tissue electrophysiology simulators using an N-version benchmark. *Philosoph. Trans. R. Soc. A Math. Phys. Eng. Sci.* 369 (1954), 4331–4351. <https://doi.org/10.1098/rsta.2011.0139>.
- Ono, N., Yamaguchi, T., Ishikawa, H., Arakawa, M., Takahashi, N., Saikawa, T., Shimada, T., 2009. Morphological varieties of the Purkinje fiber network in mammalian hearts, as revealed by light and electron microscopy. *Arch. Histol. Cytol.* 72 (3), 139–149. <https://doi.org/10.1679/aohc.72.139>.
- Passini, E., Britton, O.J., Lu, H.R., Rohrbacher, J., Hermans, A.N., Gallacher, D.J., Greig, R.J.H., Bueno-Orovio, A., Rodríguez, B., 2017. Human in silico drug trials demonstrate higher accuracy than animal models in predicting clinical pro-arrhythmic cardiotoxicity. *Front. Physiol.* 8. <https://www.frontiersin.org/articles/10.3389/fphys.2017.00668>.
- Roney, C.H., Sim, I., Yu, J., Beach, M., Mehta, A., Alonso Solis-Lemus, J., Kotadia, I., Whitaker, J., Corrado, C., Razeghi, O., Vigmond, E., Narayan, S.M., O'Neill, M., Williams, S.E., Niederer, S.A., 2022. Predicting atrial fibrillation recurrence by combining population data and virtual cohorts of patient-specific left atrial models. *Circ. Arrhythm. Electrophysiol.* 15 (2), e010253 <https://doi.org/10.1161/CIRCEP.121.010253>.
- Rosen, M.R., Legato, M.J., Weiss, R.M., 1981. Developmental changes in impulse conduction in the canine heart. *Am. J. Physiol.-Heart Circ. Physiol.* 240 (4), H546–H554. <https://doi.org/10.1152/ajpheart.1981.240.4.H546>.
- Sachetto Oliveira, R., Martins Rocha, B., Burgarelli, D., Meira Jr., W., Constantinides, C., Weber dos Santos, R., 2018. Performance evaluation of GPU parallelization, space-time adaptive algorithms, and their combination for simulating cardiac electrophysiology. *Int. J. Numer. Method. Biomed. Eng.* 34 (2), e2913. <https://doi.org/10.1002/cnm.2913>.
- Schäufelberger, M., Schuler, S., Bear, L., Cluitmans, M., Coll-Font, J., Onak, Ö.N., Dössel, O., Brooks, D., 2019. Comparison of activation times estimation for potential-based ECG imaging. *Comput. Cardiol.* 2010, 46. <https://doi.org/10.22489/cinc.2019.379>.
- Schuler, S., Piliä, N., Potyagaylo, D., Loewe, A., 2021. Cobivoco: consistent biventricular coordinates for precise and intuitive description of position in the heart – with MATLAB implementation. *Med. Image Anal.* 74, 102247 <https://doi.org/10.1016/j.media.2021.102247>.
- Serinagaoglu Dogrusoz, Y., Bear, L., Bergquist, J., Dubois, R., Good, W., MacLeod, R., Rababah, A., Stoks, J., 2019. Effects of interpolation on the inverse problem of electrocardiography. In: *Proceedings of the Computing in Cardiology Conference*. <https://doi.org/10.22489/CinC.2019.100>.
- Streeter, D.D., Spotnitz, H.M., Patel, D.P., Ross, J., Sonnenblick, E.H., 1969. Fiber orientation in the canine left ventricle during diastole and systole. *Circ. Res.* 24 (3), 339–347. <https://doi.org/10.1161/01.RES.24.3.339>.
- Sudlow, C., Gallacher, J., Allen, N., Beral, V., Burton, P., Danesh, J., Downey, P., Elliott, P., Green, J., Landray, M., Liu, B., Matthews, P., Ong, G., Pell, J., Silman, A., Young, A., Sprosen, T., Peakman, T., Collins, R., 2015. UK Biobank: an open access resource for identifying the causes of a wide range of complex diseases of middle and old age. *PLoS Med.* 12 (3) <https://doi.org/10.1371/journal.pmed.1001779>.
- Taggart, P., Sutton, P.M., Ophof, T., Coronel, R., Trimlett, R., Pugsley, W., Kallis, P., 2000. Inhomogeneous transmural conduction during early ischaemia in patients with coronary artery disease. *J. Mol. Cell. Cardiol.* 32 (4), 621–630. <https://doi.org/10.1006/jmcc.2000.1105>.
- Tomek, J., Bueno-Orovio, A., Passini, E., Zhou, X., Mincholé, A., Britton, O., Bartolucci, C., Severi, S., Shrier, A., Virag, L., Varro, A., Rodríguez, B., 2019. Development, calibration, and validation of a novel human ventricular myocyte model in health, disease, and drug block. *Elife* 8, e48890. <https://doi.org/10.7554/eLife.48890>.
- Trovato, C., Passini, E., Nagy, N., Varró, A., Abi-Gerges, N., Severi, S., Rodríguez, B., 2020. Human Purkinje in silico model enables mechanistic investigations into automaticity and pro-arrhythmic abnormalities. *J. Mol. Cell. Cardiol.* 142, 24–38. <https://doi.org/10.1016/j.yjmcc.2020.04.001>.
- Vigmond, E.J., Stuyvers, B.D., 2016. Modeling our understanding of the His-Purkinje system. *Prog. Biophys. Mol. Biol.* 120 (1), 179–188. <https://doi.org/10.1016/j.pbiomolbio.2015.12.013>.
- Wallman, M., Smith, N.P., Rodríguez, B., 2012. A comparative study of graph-based, eikonal, and monodomain simulations for the estimation of cardiac activation times. *IEEE Trans. Biomed. Eng.* 59 (6), 1739–1748. <https://doi.org/10.1109/TBME.2012.2193398>.
- Wiedmann, R.T., Tan, R.C., Joyner, R.W., 1996. Discontinuous conduction at Purkinje-ventricular muscle junction. *Am. J. Physiol.-Heart Circ. Physiol.* 271 (4), H1507–H1516. <https://doi.org/10.1152/ajpheart.1996.271.4.H1507>.
- Yokoshiki, H., Mitsuyama, H., Watanabe, M., Mizukami, K., Tsutsui, H., 2014. Suppression of ventricular fibrillation by electrical uncoupling of the Purkinje system in hypertrophic cardiomyopathy. *Heart Vessels* 29 (5), 709–717. <https://doi.org/10.1007/s00380-013-0423-1>.
- Zacur, E., Mincholé, A., Villard, B., Carapella, V., Ariga, R., Rodríguez, B., Grau, V., 2017. MRI-based heart and torso personalization for computer modeling and simulation of cardiac electrophysiology. In: Cardoso, M.J., Arbel, T., Tavares, J.M.R.S., Aylward, S., Li, S., Boctor, E., Fichtinger, G., Cleary, K., Freeman, B., Kohli, L., Shipley Kane, D., Oetgen, M., Pujol, S. (Eds.), *Imaging For Patient-Customized Simulations and Systems for Point-of-Care Ultrasound*, 10549. Springer International Publishing, pp. 61–70. https://doi.org/10.1007/978-3-319-67552-7_8.